J. Fluid Mech. (2023), *vol*. 957, A28, doi:10.1017/jfm.2022.999

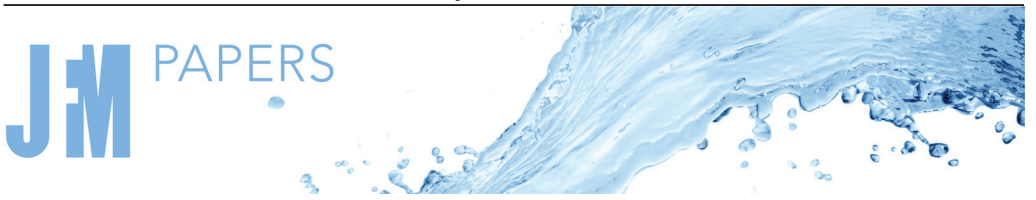

Partial cavity shedding on a hydrofoil resulting from re-entrant flow and bubbly shock waves

Anubhav Bhatt[1], **Harish Ganesh**[2,†] **and Steven L. Ceccio**[1,2]

[1]Department of Mechanical Engineering, University of Michigan, Ann Arbor, MI 48105, USA

[2]Department of Naval Architecture and Marine Engineering, University of Michigan, Ann Arbor, MI 48105, USA

(Received 3 January 2022; revised 25 September 2022; accepted 2 November 2022)

Partial cavity flows forming on a NACA0015 hydrofoil are visualized using high-speed cinematography and time-resolved X-ray densitometry. These observations reveal the underlying flow features that lead to the cloud cavity shedding. Previous studies have reported that both near-surface liquid re-entrant flow and bubbly shock waves can serve as the mechanisms causing cavity pinch-off and cloud shedding. We identify both mechanisms in the current study. The cavity shedding frequency was also examined and related to the underlying flow dynamics. The probability of re-entrant flow or bubbly shock-induced shedding processes are quantified, and the likelihood of each mechanism is shown to be a function of both the cavitation number and the Mach number of the bubbly mixture within the separated region of the cavity. When the Mach number of the two-phase mixture in the cavity exceeds unity, shock waves become the dominant mechanism that lead to large-scale cavity shedding and cloud cavitation.

Key words: cavitation, multiphase flow, gas/liquid flow

1. Introduction

Understanding the physical mechanisms leading to partial cavity shedding is important for the modelling and control of cavitation dynamics. Cloud cavitation that results from partial cavity shedding can have deleterious effects on the performance of hydraulic systems such as pumps, propulsors and hydrodynamic control surfaces. Partial cavities can form in regions of separated flow that detach and close on a lifting surface. While such cavities may have a relatively stable streamwise length, they can transition to flows that periodically shed large quantities of vapour, forming cloud cavitation. The classical explanation for the development of this cavitation instability is attributed to the presence of a liquid re-entrant jetting flow that forms near the closure of the partial cavity (Knapp 1955; Furness & Hutton

† Email address for correspondence: gharish@umich.edu

© The Author(s), 2023. Published by Cambridge University Press. This is an Open Access article, distributed under the terms of the Creative Commons Attribution licence (http://creativecommons.org/licenses/by/4.0), which permits unrestricted re-use, distribution and reproduction, provided the original article is properly cited.

https://doi.org/10.1017/jfm.2022.999 Published online by Cambridge University Press

1975). When the pocket of flow separation is closed on the solid flow boundary, a flow of near-surface liquid travelling upstream is created underneath the cavity, as reviewed by Franc (2001).

The study of partial cavity dynamics has often focused on the flow around stationary hydrofoils. In one of the earliest studies, Wade & Acosta (1966) presented the dependence of lift and drag experienced by a plano-convex hydrofoil when experiencing partial and cloud cavitation. Since then, many studies have been carried out to understand the effect of large-scale cavity formation and shedding on the performance characteristics of the hydrofoils. The formation of re-entrant cavity flows has been examined experimentally by several researchers on nominally two-dimensional test articles (Le, Franc & Michel 1993; Kawanami *et al.* 1997; Pham, Larrarte & Fruman 1999; Gopalan & Katz 2000; Callenaere *et al.* 2001; Laberteaux & Ceccio 2001*a*; Leroux, Astolfi & Billard 2004; Leroux, Coutier-Delgosha & Astolfi 2005; Coutier-Delgosha *et al.* 2007) and on objects with spanwise variation (De Lange & De Bruin 1997; Laberteaux & Ceccio 2001*b*; Smith *et al.* 2020). The passive control of partial cavity shedding on hydrofoils has been attempted by placing obstacles on the expected path of the liquid re-entrant flow (Kawanami *et al.* 1997).

Le *et al.* (1993) suggested a scaling for the dynamics associated with re-entrant flow shedding where the Strouhal number based on the cavity length is given by

$$St_L = \frac{fL_C}{u_0} \sim \frac{1}{3}, \tag{1.1}$$

where f is the shedding frequency, u_0 is the free-stream speed that is assumed to be on the same order as the re-entrant flow speed and L_C is the maximum cavity length. The value of 1/3 results from the presumption of a three-step process: cavity growth to maximum length, re-entrant flow convection beneath the partial cavity and cavity break-off after the flow impinges on the line of cavity detachment. Callenaere *et al.* (2001) showed that the re-entrant flow speed is often lower than the free-stream speed, making the constant $\sim$1/4, when the re-entrant flow speed is roughly half the free-stream speed. With this scaling there is no dependence of St_L with cavitation number σ, even though the cavity length increases with decreasing cavitation σ. Instead, the scaling predicts a corresponding decrease in the shedding frequency, f. Such scaling has qualitatively predicted the shedding frequency on two-dimensional hydrofoils for cavities with mean lengths that are relatively short compared with the streamwise extent of the cavitating object (i.e. the chord of a hydrofoil).

Arndt *et al.* (2000) and Kjeldsen, Arndt & Effertz (2000) identified two distinct shedding regimes as they examined partial cavitation on a two-dimensional hydrofoil. The first regime was designated as type 2 for incipient and developing partial cavities, in which the characteristic St_C was dependent on σ. In their scaling of the frequency, they used the hydrofoil chord, C, to define St. Thus, dependence of St_C with σ mainly results from the increase in the mean cavity length with decreasing cavitation number. The second regime they designated as type 1 for developed partial cavities. For type 2 cavities, the shedding process abruptly changed, exhibiting a sharp reduction in St_C that was insensitive to σ. Similar behaviour was also observed by Leroux *et al.* (2004, 2005). Arndt *et al.* (2000) hypothesized that a shock wave created by the collapsing shed cloud of the previous cycle might be instigating the collapse of the attached cavity forming upstream. In addition to these large features, Arndt (2012) also suggested that the presence of vortex shedding at the hydrofoil trailing edge could play a role in the observed cavity shedding process.

Recent investigations employing cinematographic X-ray densitometry of cavitating flows have identified a second mechanism that leads to cavity dynamics that result

https://doi.org/10.1017/jfm.2022.999 Published online by Cambridge University Press

in large-scale cloud cavitation apart from liquid re-entrant flows. The formation and propagation of bubbly shock waves have been observed as the other mechanism of cavity shedding, and their presence can have a profound impact on the cavity shedding process. Partial cavities are often comprised of a high void fraction bubbly mixture, making this region of the flow highly compressible compared with the pure liquid and vapour phases. These flows can have sound speeds much slower than the liquid convection speeds, making them locally supersonic. Experimental studies by Ganesh, Makiharju & Ceccio (2016), Jahangir, Hogendoorn & Poelma (2018), Barbaca *et al.* (2019), Petkovšek, Hočevar & Dular (2020) and Bhatt, Ganesh & Ceccio (2021), along with numerical studies by Budich, Schmidt & Adams (2018), Bhatt & Mahesh (2020) and Trummler, Schmidt & Adams (2020) show that propagating bubbly shock waves can occur in separated cavitating flows and can dominate the process that leads to large-scale cavity shedding.

Wu, Ganesh & Ceccio (2019) and Barwey *et al.* (2020) studied partial cavitation on a two-dimensional NACA0015 hydrofoil with uniform span, similar to the geometry employed by Arndt *et al.* (2000), and observed the basic behaviour of the partial cavitation reported in the previous work. However, by employing X-ray densitometry, they reported a wider variety of cavity shedding processes that were distinct from the classical re-entrant flow mechanism. They found propagating bubbly shock waves to be a cause of cavity pinch-off at lower cavitation numbers. They also found that the shedding process occurred over multiple steps, often influenced by the pressure wave produced by the collapse of shed clouds. Under conditions close to transition from type 2 to type 1 (similar classification as Kjeldsen *et al.* 2000), the shedding was multi-modal, exhibiting a two- or three-step process with abrupt transitions. Using data-driven analysis of time-varying void fraction fields, Barwey *et al.* (2020) confirmed that this transition process was related to the collapse of vapour clouds near the trailing edge of the hydrofoil. They found that the observed shedding dynamics matched the trend reported by Kjeldsen *et al.* (2000), and relevant flow structures and processes were identified.

Despite a thorough study, Wu *et al.* (2019) were not able to quantitatively identify the presence of re-entrant liquid flow using X-ray densitometry measurements, given the limits of their flow visualization near the surface of the hydrofoil. In addition, their lack of surface pressure measurements, both steady and unsteady, prevented the assessment of the partial cavity mixture properties, such as the local speed of sound and the pressure rise across the convecting shock fronts. Thus, the interplay between re-entrant flows and bubbly shock waves as the mechanism for the observed cavity dynamics remained hidden. While numerical modelling suggests that the simultaneous formation of both liquid re-entrant flows and bubbly shock waves are possible (Bhatt & Mahesh 2020; Trummler *et al.* 2020), the relative importance of each mechanism at any given flow condition is still a topic of interest, especially given the complex flow dynamics observed on relatively simple test articles.

In the present study we seek to explore the flow conditions within the cavity that result in the formation of both re-entrant flows and bubbly shock fronts. In particular, we examine the interplay of both shedding mechanisms and determine the conditions under which re-entrant flow or bubbly shock propagation may dominate the shedding process. To do this, we continue to examine the cavitating flow on a NACA0015 hydrofoil. However, in the present study, the test model is larger than the one employed by Wu *et al.* (2019) and similar to those investigated by Arndt *et al.* (2000). This allows us to visualize the presence of near-surface liquid re-entrant flow. The larger size also allows us to place static pressure ports and unsteady surface pressure transducers on the foil surface, providing measurements of the time-synchronous pressure and void fraction variations of the partial

https://doi.org/10.1017/jfm.2022.999 Published online by Cambridge University Press

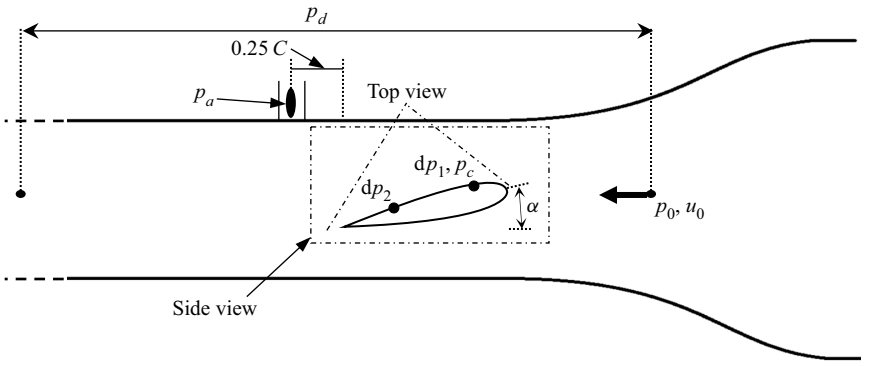

Figure 1. Schematic of NACA0015 hydrofoil mounted in the water tunnel with top and side views used for high-speed videography highlighted. For void fraction measurements, we have a 135 mm by 85 mm field of view covering roughly 80 % of the chord. To visualize the cavitation at the trailing edge, the X-ray field of view was moved downstream. Surface pressure measurements on the suction side of the hydrofoil were made at dp_1, dp_2 and p_c. The overall pressure drop across the test section, p_d, was also measured.

cavity. The resulting data allows for the identification of both liquid re-entrant flows as well as bubbly shock waves for different cavitation numbers and attack angles, permitting us to determine the conditions under which either (or both) shedding mechanism exists and their associated cavity dynamics.

2. Experimental set-up

Experiments were performed at the University of Michigan 9-inch re-circulating water tunnel. The test section is 1 m long with a circular inlet of 0.23 m in diameter that smoothly transitions into a square test section with a cross-section of 0.21 × 0.21 m with rounded corners. Honeycombs and screens upstream of the test section ensure flow straightening and low free-stream turbulence levels (<2 %). The inlet speed u_0 and the inlet pressure p_0 can be varied from 0 to 15 m s^{-1} and from near vacuum to 200 kPa absolute pressure. A symmetric two-dimensional hydrofoil (NACA0015) model was made from brass with a chord, C, of 165.6 mm and a span of 209.6 mm resulting in an aspect ratio of 1.27. A schematic of the hydrofoil mounted in the test section is shown in figure 1. Experiments were performed at attack angles of $\alpha = 7^\circ$ and $\alpha = 10^\circ$.

The inlet velocity, u_0, was determined from the measured pressure drop across the contraction using a Setra 230, 0–68 kPa, differential pressure transducer with an accuracy of 0.25 % of full scale. Inlet static pressure, p_0, was measured using Omega PX409-030A5V, 0 to 206 kPa static pressure transducer (0.08 % full scale accuracy). The overall pressure drop across the test section, p_d, was also measured using Omega RX2300, 0–34 kPa (0.25 % full scale accuracy) differential pressure transducer, and this value ranged from 7.5 to 12 kPa for $\alpha = 7^\circ$, and 9–15 kPa for $\alpha = 10^\circ$. For the present experiments, p_0 was varied from 35.0 to 120.0 kPa (±0.2 kPa) for a fixed $u_0 = 8.00 \pm 0.14$ m s^{-1} to achieve a range of inlet cavitation numbers, σ_0, calculated using

$$\sigma_0 = \frac{p_0 - p_v}{\frac{1}{2}\rho u_0^2}, \tag{2.1}$$

where p_v and ρ are the liquid vapour pressure and density at room temperature, respectively. The resulting range of cavitation numbers examined was $1.00 < \sigma_0 < 3.70$

https://doi.org/10.1017/jfm.2022.999 Published online by Cambridge University Press

(±0.07). The Reynolds number based on the hydrofoil chord is 1.3 million. For all the experiments, the dissolved oxygen content was maintained below 15 % of saturation at atmospheric pressure, and the liquid temperature ranged from 20 °C to 23 °C.

The surface static pressure, p_c, and unsteady surface pressures, $\mathrm{d}p_1$ and $\mathrm{d}p_2$, on the suction side of the hydrofoil were measured at locations shown in figure 1. The static pressure was measured via a 1.6 mm diameter pressure port 40.6 mm away from the leading edge of the foil through a Omega PX409-110 005AI-EH (0–34 kPa with 0.08 % full scale accuracy) static pressure transducer. Unsteady surface pressures were measured using two PCB 113M231 CVLD unsteady pressure transducers. The pressure sensor diaphragm had a diameter of 5.54 mm. The transducer $\mathrm{d}p_1$ had charge sensitivity of 7.59 μA kPa^{-1} at 0.2 % full scale linearity, while the transducer used to measure $\mathrm{d}p_2$ had 7.28 μA kPa^{-1} charge sensitivity at 0.1 % full scale linearity. Unsteady pressure signals were acquired at a frequency of 50(or 100) kHz for a duration of 3(or 2) s. The emitted acoustic pressure, p_a, was measured using a Brüel and Kjær submersible hydrophone (no. 2241694) with a voltage sensitivity of 26.3 μV kPa^{-1}. The hydrophone was mounted outside the tunnel above the top window of the test section in a water pocket located at 41.4 mm from the hydrofoil trailing edge. The hydrophone signal was acquired at 100 kHz for a duration of 2 s.

The static and unsteady pressure measurements were made synchronous with the high-speed videos and X-ray densitometry measurements. The top and side views of cavitating events were observed using two Phantom v710 cameras at 7500 fps for 1.5 s. The location of cameras and their fields of view are shown in figure 1. For the top-view camera a Nikon AF-P DX NIKKOR 18–55 mm f/3.5–5.6 G VR zoom lens was used, while for the side-view camera, a Nikon Micro-NIKKOR-P 55 mm f/3.5–32 lens was used. The two cameras and the data acquisition for the pressure measurements were triggered using a TTL signal generated by a Stanford DG535 delay generator. X-ray densitometry measurements of time-resolved, spanwise-averaged void fraction fields, $\beta(x, y, t)$, were obtained at 1 kHz for 0.787 s for a spatial resolution of 0.125 mm, using a Varian medical X-ray source and a scintillating detector with an image intensifier. Mäkiharju *et al.* (2013*a*) and Mäkiharju, Perlin & Ceccio (2013*b*) discuss this time-resolved X-ray densitometry system in detail. The measurement uncertainty in β was ±2 % for instantaneous and ±0.5 % for time-averaged measurements.

3. Cavity topology and shedding dynamics

In this section we will examine the basic topology and dynamics of the partial cavity flows as they occur with varying pressure and attack angle, by dividing the flow into four distinct regimes. Delineation of the regimes is based on the mean cavity length and the frequency of cavity shedding. Table 1 shows the four regimes of cavitation observed and their associated features. Definitions of types (i)–(iv) in the current study are not based on the type 1 and type 2 definitions of Kjeldsen *et al.* (2000). The mean partial cavity length and shedding frequency vary as a function of cavitation number for a given angle of attack. Data from the present experiments are also compared with previous results from Arndt *et al.* (2000) and Wu *et al.* (2019). Arndt *et al.* (2000) report visual cavity length data taken at two different facilities (denoted as 'Arndt' and 'Obernach'). Figure 2 shows the mean cavity length, L_C, determined from both high-speed videos and X-ray densitometry based void fraction measurements using the method of Wu *et al.* (2019). For periodically shedding cavities, the average of the maximum cavity length was designated as L_C in the high-speed images shown in figure 2(*a*). In the time-averaged void fraction fields the

https://doi.org/10.1017/jfm.2022.999 Published online by Cambridge University Press

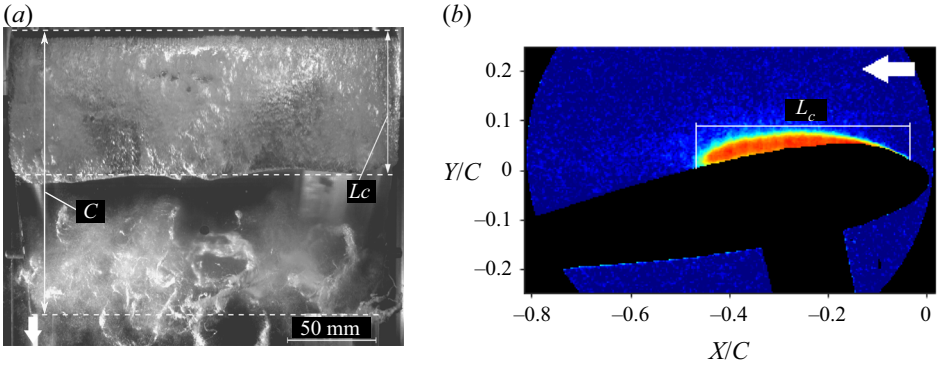

Figure 2. Determination of cavity length (L_C) from (*a*) a snapshot from a high-speed video (HS) and (*b*) the average void fraction field (XR). The colours represent the void fraction values in the range 0–0.5. Here $\sigma_0 = 2.6$, $\alpha = 10^\circ$.

Cavity type	$\sigma_0/2\alpha$	Cavity length	Dominant flow features
(i)	9.2–7.6	$0.2 < L_C/C \leq 0.4$	Re-entrant flow induced cavity pinch-off
(ii)	7.6–6.1	$0.4 < L_C/C \leq 0.6$	Both re-entrant flow and bubbly shock waves cause cavity pinch-off
(iii)	6.1–5.1	$0.6 < L_C/C \leq 0.85$	Bubbly shock wave dominated
(iv)	<5.1	$L_C/C > 0.85$	Shock wave dominated shedding with trailing edge cavitation

Table 1. Categorization of four different cavity shedding regimes observed on the NACA0015 hydrofoil. The type (i)–(iv) cavity nomenclature is different form the type 1 and type 2 cavity classification used by Kjeldsen *et al.* (2000).

maximum cavity length was measured from the separation line near the leading edge to the location of $\beta < 0.05$, as shown in figure 2(*b*). Both the cavity length and the shedding frequency, f, varied with the inlet cavitation number, σ_0, and the attack angle, α. It is useful to present these data as a function of $\sigma_0/2\alpha$.

Cavitation inception occurred on the suction side of the hydrofoil near the leading edge at $\sigma_0/2\alpha = 10.8$. With a further reduction in $\sigma_0/2\alpha$, stable cavities grew in length until $L_C/C \approx 0.2$. At lower $\sigma_0/2\alpha$, stable sheet cavities transitioned to shedding cavities. Upon further reduction, both the cavity length and thickness increased for the shedding cavities. When the cavity length $L_C/C > 0.65$, interaction between the shed cloud and cavitation forming near the trailing edge was observed. Figure 3 shows the cavity length, L_C, varying with $\sigma_0/2\alpha$, and the shedding cavity regimes summarized in table 1. Also included are data reported by Wu *et al.* (2019) and Arndt (2012). To compare the changes in L_C from different studies, a velocity based blockage correction using the following equation was made:

$$\sigma_0 = \frac{\lambda_0^2}{\lambda_P^2}\sigma_P. \tag{3.1}$$

Here, λ is the area blockage of the model in the test section at a given attack angle, and the subscripts '0' and 'P' correspond to current and previous studies, respectively. The '0' condition is $\alpha = 10^\circ$ from the current study. The value of $(\lambda_0/\lambda_P)^2$ was 1.47 for the Wu

https://doi.org/10.1017/jfm.2022.999 Published online by Cambridge University Press

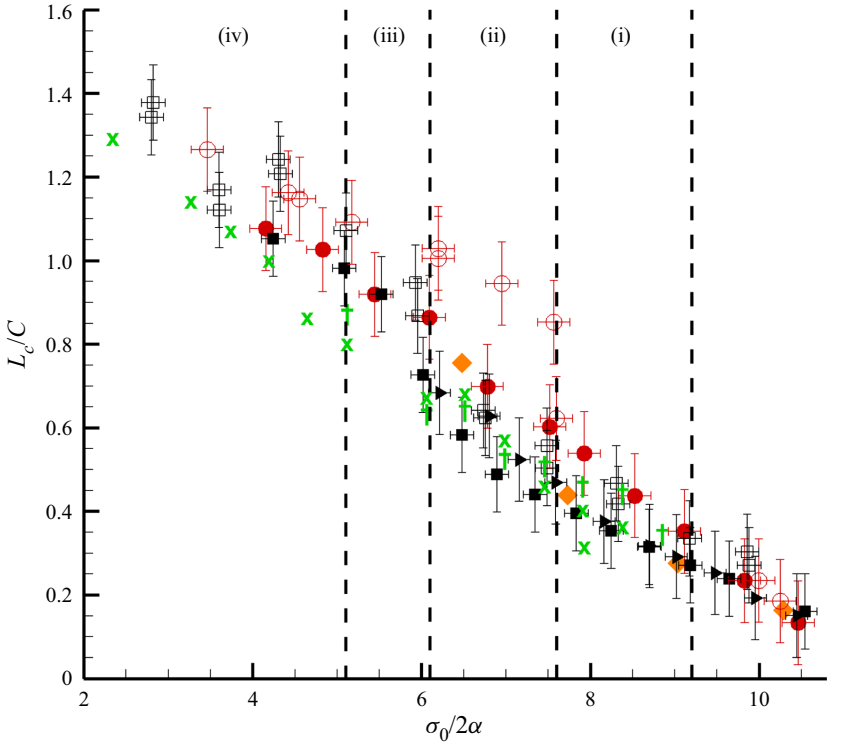

Figure 3. Variation in cavity length (L_C/C) with cavitation parameter ($\sigma_0/2\alpha$) measured in the current NACA0015 hydrofoil, compared with the previous studies. Two angles of attack used in the current study are $\alpha = 10^\circ$ (■, from high-speed videos; ▶, from X-ray measurements) and $\alpha = 7^\circ$ (red circle, from high-speed videos) at $u_0 = 8$ m s^{-1}. Measurements from the current study (filled symbols) are compared with those observed by Wu *et al.* (2019) ($\alpha = 10^\circ$, □; 7°, ◯ from high-speed videos) at $u_0 = 8$ m s^{-1}. Arndt *et al.* (2000) reported data from Obernach for $\alpha = 8^\circ$ at $u_0 = 8$ m s^{-1}, green dagger and $u_0 = 10$ m s^{-1}, green multiple symbol. They also presented data from their own facility for $\alpha = 7^\circ$ at $u_0 = 8$ m s^{-1}, orange diamond (both blockage corrected). Lines of demarcation of the observed cavitation regimes (types (i) through (iv)) are also shown.

et al. (2019) data, 1.30 for the Arndt data and 1.20 for the Obernach data from Arndt *et al.* (2000). The cavity length increases with decreasing cavitation number, and the data from the present and previous experiments are consistent, and scale with $\sigma_0/2\alpha$.

The cavity shedding frequency was determined from the two flush mounted unsteady pressure transducers dp_1 and dp_2, and time-resolved X-ray densitometry measurements. To estimate the dominant frequencies, f, from X-ray densitometry measurements, a time series of the spatial average of the void fraction within a probe volume located at the cavity closure, β_{L_C} was analysed. The locations of dp_1 and dp_2 and the void fraction probe are shown in figures 4(*a*) and 4(*b*), respectively. A sample time trace of the dynamic pressure signal, dp_1, near the leading edge of the foil for a type (ii) cavity is shown in figure 5(*a*). The corresponding power spectral density ($\widehat{\text{PSD}}$, PSD normalized by peak value) curve for the signal is shown in figure 5(*b*). Similarly, time traces and corresponding $\widehat{\text{PSD}}$ curves for dp_2 and β_{L_C} are shown in figure 5(*c–f*). A single dominant shedding frequency is seen from the pressure and void fraction signals in figure 5. The raw time signals and corresponding $\widehat{\text{PSD}}$ curves for a type (iv) cavity are shown in figure 6. The observed dominant frequencies

https://doi.org/10.1017/jfm.2022.999 Published online by Cambridge University Press

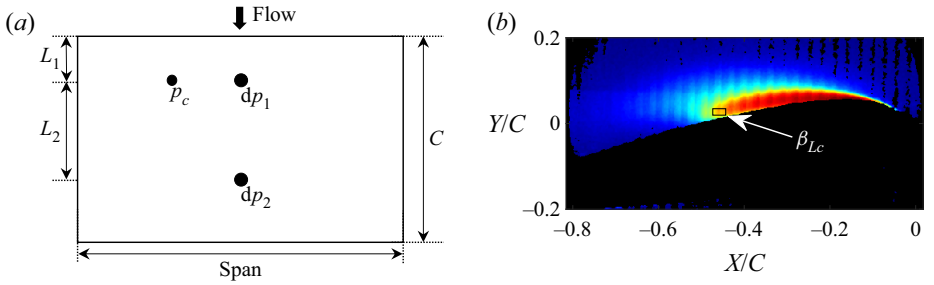

Figure 4. Schematic showing the locations of the dynamic surface pressure measurement locations measuring dp_1 and dp_2 on the suction side of the hydrofoil at $L_1 = 40.6$ mm and $L_2 = 69.8$ mm (*a*), and the location of the void fraction probe near the maximum cavity length to measure β_{L_C} (*b*). The probe area was a rectangular window, 5 mm by 2.5 mm, and it was placed at the location of the maximum cavity length determined from the mean void fraction field.

were non-dimensionalized to define the Strouhal number based on the chord length using

$$St_C = \frac{fC}{u_0}. \tag{3.2}$$

A few type (ii) cavities, and all type (iii) and type (iv) cavities exhibited two dominant frequency peaks in their PSDs. The number of peaks detected by the pressure transducers dp_1 and dp_2 depended on the cavity length and the nature of the shedding cycle. Longer cavities covered the upstream sensor with vapour, preventing dp_1 from detecting pressure changes occurring at the cavity closure. Similarly, the downstream sensor was often not able to detect meaningful pressure at lower cavity lengths. Both these transducers were able to detect signal changes when the cavity closure was close to their locations. To measure variations at the cavity closure, a spatially averaged void fraction probe at the cavity closure, β_{L_C}, was chosen to compare with the pressure signals. Figure 7 shows the first and second dominant peaks in St_C from the β probe at the cavity closure, β_{L_C}, along with the surface pressure signals for $\alpha = 7^\circ$ and 10°. The St_C peaks inferred from β probes compare well with the dominant peaks seen in pressure transducer signals dp_1 and dp_2. Also, the St_C for the hydrofoil at $\alpha = 10^\circ$ is greater than that for $\alpha = 7^\circ$. The trend observed in the variation of St_C based on the first peak is similar to that reported by Arndt (2012) and Kjeldsen *et al.* (2000), which are superimposed with the present results in figure 7(*a*). The first peak in St_C is observed to decrease monotonically with decreasing σ_0 until $\sigma_0/2\alpha \approx 6.1$ where type (iii) cavities begin to occur.

At higher cavitation numbers, $\sigma_0/2\alpha > 9.2$, a steady sheet cavity forms that is shorter and thinner than the type (i) cavities. Both the pressure and void fraction signals are broadband for these cavities and no dominant peak in the range of $0 < St_C < 1.5$ is observed. As the cavity length increases, St_C decreases below 1 for both pressure and void fraction signals. Two frequency peaks are observed for longer type (ii) shedding cavities. The second dominant peak is detected for type (ii) cavities at $\sigma_0/2\alpha < 7.2$ ($\alpha = 10^\circ$), as shown in figure 7(*c*,*d*). At the onset of type (iii) cavities, the variation in St_C with decreasing $\sigma_0/2\alpha$ (gradient of St_C with $\sigma_0/2\alpha$) is reduced, following a similar trend reported by Kjeldsen *et al.* (2000). This trend is observed in the first dominant peak measured for both type (iii) and type (iv) cavities. The monotonic trend in the dominant and secondary peak in St_C, present until $\sigma_0/2\alpha \sim 6.1$ (figure 7*a*,*c*), diminishes when L_C is used as a characteristic length in determining St_{L_C} (figure 7*b*,*d*).

https://doi.org/10.1017/jfm.2022.999 Published online by Cambridge University Press

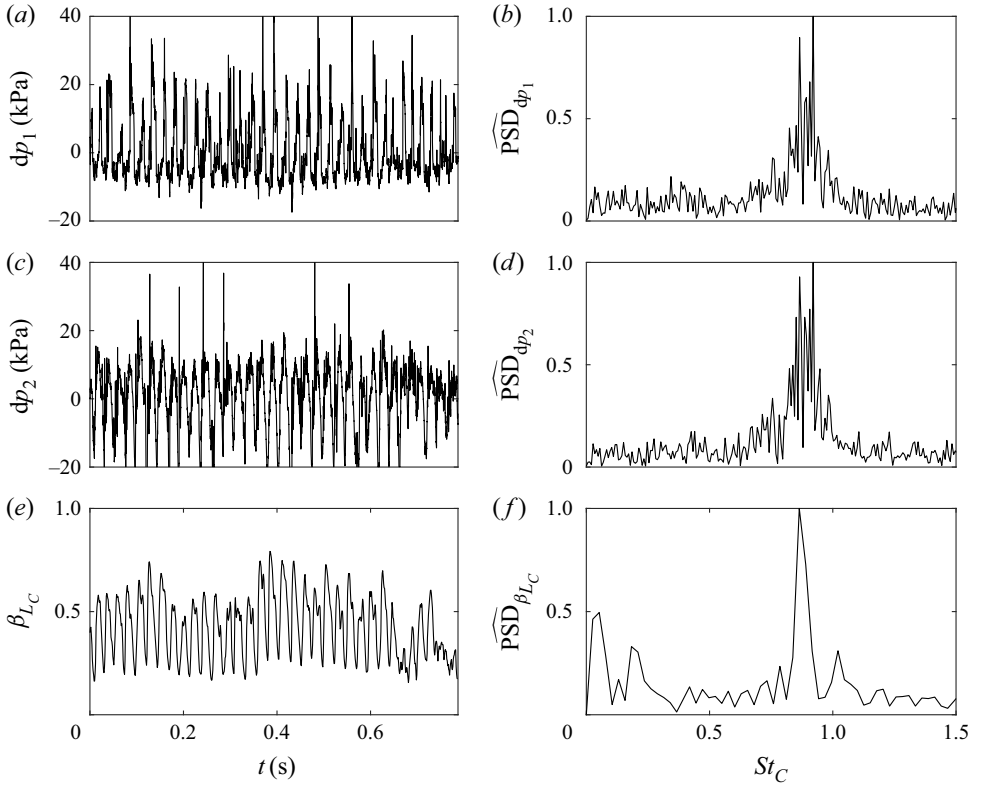

Figure 5. Time-varying signals and the corresponding normalized power spectral density variation $\widehat{\mathrm{PSD}}$ for each of the surface pressure transducers and the void fraction probe. Plots (*a*), (*c*) and (*e*) are the raw time signals for $\mathrm{d}p_1$, $\mathrm{d}p_2$ and β_{L_C}, respectively. Plots (*b*), (*d*) and (*f*) are the corresponding $\widehat{\mathrm{PSD}}$ data. The signals are presented for a type (ii) shedding cavity at $\sigma_0/2\alpha = 7.6$ and $\alpha = 10^\circ$.

Type	$\sigma_0/2\alpha$	L_C/C	Dominant flow features
(i)	9.0	0.29	Liquid re-entrant flow
(ii)	7.5	0.47	Liquid re-entrant flow + bubbly shock waves
(iii)	5.4	0.92	Shock wave dominant
(iv)	4.1	1.05	Bubbly shock waves + trailing edge cavitation

Table 2. The four cases demonstrating the different flow regimes, all at $\alpha = 10^\circ$.

A more detailed examination of the void fraction flow fields and high-speed videos for four representative cases of types (i)–(iv) is presented in the upcoming section. Table 2 presents four cases that we will examine in detail below, representative of the four cavity types. The selected conditions are at $\alpha = 10^\circ$, since cavities forming at $\alpha = 7^\circ$ and at lower σ_0 can exhibit three dimensionality that makes interpretation of the X-ray densitometry measurements more challenging.

https://doi.org/10.1017/jfm.2022.999 Published online by Cambridge University Press

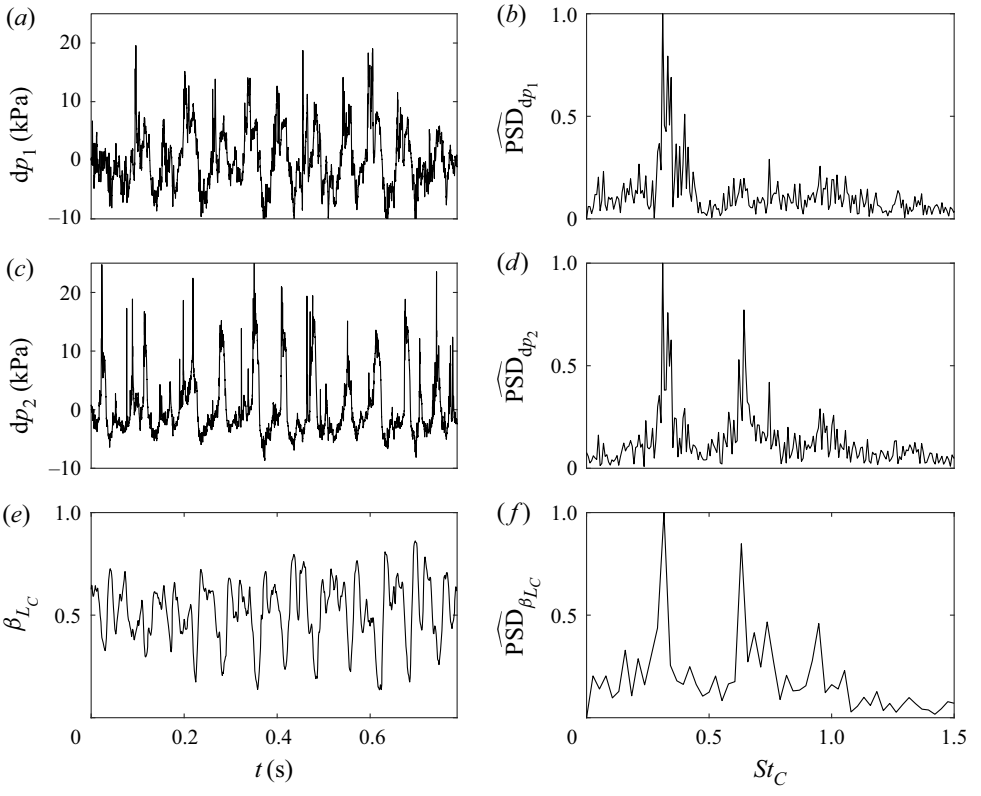

Figure 6. Time-varying signals and the corresponding normalized power spectral density variation $\widehat{\mathrm{PSD}}$ for each of the surface pressure transducers and the void fraction probe. Plots (*a*), (*c*) and (*e*) are raw time signals for $\mathrm{d}p_1$, $\mathrm{d}p_2$ and β_{L_C}, respectively. Plots (*b*), (*d*) and (*f*) are the corresponding $\widehat{\mathrm{PSD}}$ data. The signals are presented for a type (iv) shedding cavity at $\sigma_0/2\alpha = 4.1$, $\alpha = 10^\circ$. The highest peak in St_C and the second highest peak are recorded and reported in figure 7.

4. Oscillating cavity with re-entrant flow: type (i)

Type (i) cavities experience oscillations in cavity length and exist for $9.2 > \sigma_0/2\alpha > 7.6$ with $0.2 < L_C/C < 0.4$. Type (i) cavities are not spanwise uniform and have a '*W*' or '*U*' shape in the spanwise direction. A time series of high-speed snapshots depicting a typical shedding cycle of a type (i) cavity is shown in figure 8. From the high-speed videos it is not possible to definitively identify the flow structure that causes cavity shedding. Time-resolved void fraction measurements of the type (i) cavity are shown in figure 9. The cycle shown begins with the cavity growing along the streamwise direction to achieve a maximum cavity length of $L_C/C \sim 0.2$, as depicted in figure 9(*a–c*). Upon reaching the maximum length, the cavity is pinched-off between (*c*)–(*e*), and a vapour cloud is shed downstream (*f*). X-ray densitometry measurements do not provide definitive information about the flow feature that causes cavity pinch-off, but they do reveal a region of high void fraction close to the hydrofoil surface.

The unsteady pressure registered by the pressure transducer $\mathrm{d}p_1$ during one cycle of the growth and collapse of the cavity is shown in figure 10. Between instances (1) and (2) shown in figure 10, the transducer surface is exposed to the surrounding liquid, resulting in a 16 kPa maximum pressure rise. During the cavity growth cycle between instances (2)–(3), vapour covers the surface of $\mathrm{d}p_1$ and the pressure drops by 19.6 kPa. When the

https://doi.org/10.1017/jfm.2022.999 Published online by Cambridge University Press

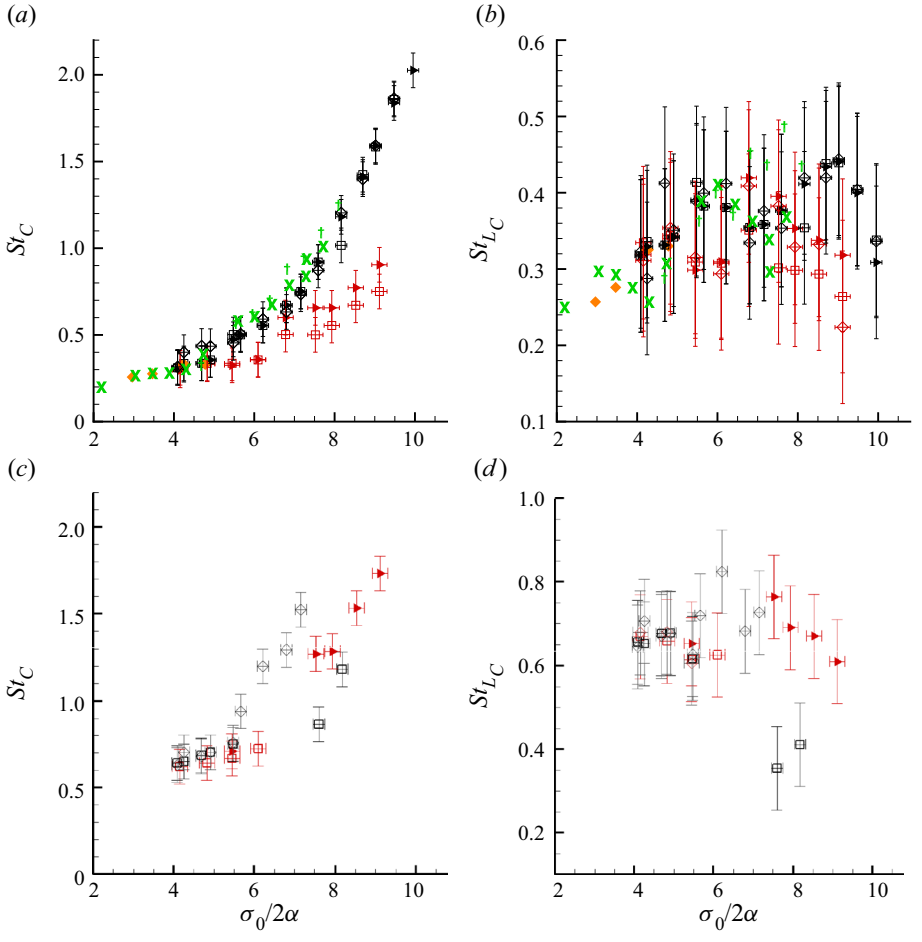

Figure 7. Variation in St with $\sigma_0/2\alpha$ for $\alpha = 7^\circ$ (red) and 10° (black). The void fraction signal (β_{L_C}) and dynamic pressure transducer signals (dp_1 and dp_2) are used to determine St. Plots (a,b) show peak 1 (dominant shedding frequency) and plots (c,d) show peak 2 (second highest peak). The signals are dp_1 (▶, red triangle right); dp_2 (□, red square); β_{L_C} (◇, red diamond). Peak 1 based St_C and St_{L_C} are compared with previous data (Arndt *et al.* 2000 for NACA0015 hydrofoil): Obernach's data, $\alpha = 8^\circ$ at $u = 8$ m s^{-1} (green dagger) and $u = 10$ m s^{-1} (green multiple symbol); Arndt's data, $\alpha = 7^\circ$ at $u = 8$ m s^{-1} (orange diamond). The σ from previous data is corrected for the difference in blockage, as shown in (3.1).

cavity pinch-off occurs between (4)–(5), the pressure drops by 6.5 kPa. Finally, as the vapour cloud convects over dp_1, a pressure rise of 9.3 kPa between (5)–(6) is recorded. For type (i) cavities, the shed vapour cloud is small and has negligible impact on subsequent cavity growth.

5. Cavity with shedding caused by re-entrant flows and bubbly shocks: type (ii)

Type (ii) cavities appear for $7.6 > \sigma_0/2\alpha > 6.1$ with $0.4 < L_C/C < 0.6$. They are characterized as exhibiting shedding due to cavity pinch-off resulting from liquid re-entrant flow and bubbly shock waves with no obvious preference for either flow front. Figure 11 illustrates a typical shedding cycle of a type (ii) cavity from top-view high-speed video snapshots. During the growth cycle shown in figure 11(a–c), a flow front (yellow

https://doi.org/10.1017/jfm.2022.999 Published online by Cambridge University Press

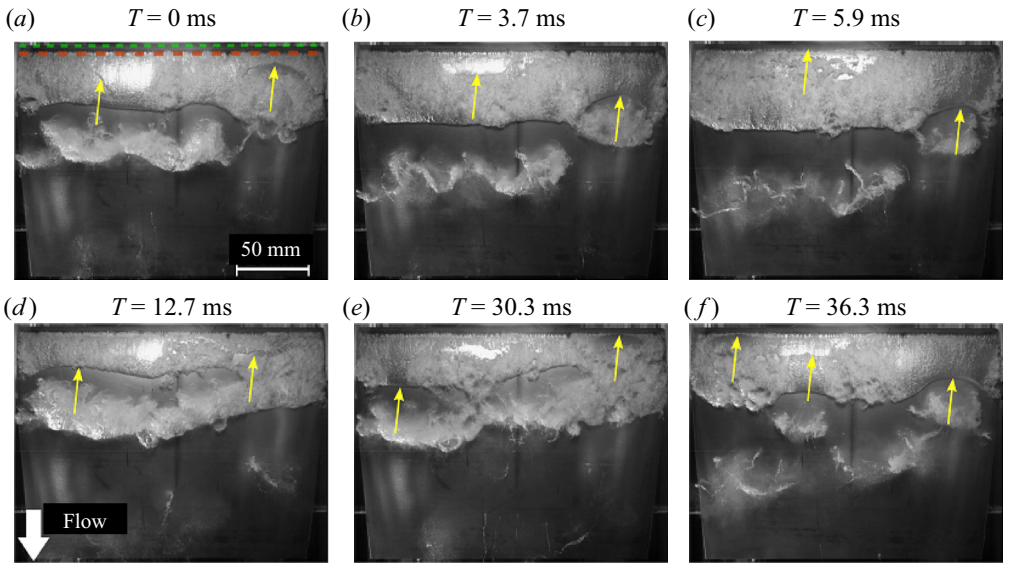

Figure 8. Images of a stable type (i) partial cavity at $\sigma_0/2\alpha = 9.2$. The arrows highlight the upstream moving flow structure underneath the cavity and the typical degree of spanwise uniformity. The cavity leading edge (orange) and the foil leading edge (green) are highlighted through dashed lines (– –) in (*a*).

arrow) near the leading edge of the hydrofoil is clearly seen. As the cavity reaches a critical length (L_c), another flow front travelling towards the leading edge (shown in red arrow) causes the cavity to pinch-off. As observed for type (i) cavities, it was not possible to identify the flow feature that causes shedding from high-speed videos. However, from time-resolved X-ray densitometry observations it was possible to identify both liquid re-entrant flow and bubbly shock-induced cavity pinch-off.

Figure 12 shows time-resolved void fraction flows of a type (ii) cavity shedding cycle caused by a re-entrant liquid flow. The shedding cycle begins with cavity growth as shown in figure 12(*a–d*). While the cavity grows, liquid accumulates underneath the cavity as shown in figure 12(*b*,*c*). This liquid flow underneath the cavity travels upstream, as shown in figure 12(*d*). Cavity pinch-off occurs near the leading edge and cloud shedding follows, as shown in figure 12(*e*,*f*). From these void fraction field measurements the flow structure responsible for the shedding is identified as a liquid re-entrant flow, visualized in figure 12(*d*).

Bubbly shock driven cavity shedding cycle for a type (ii) cavity is depicted in figure 13. The cycles begins with cavity growth and subsequent attainment of maximum length, as shown in figure 13(*a–c*). Upon attaining maximum length, the cavity begins to collapse from the rear, and a void fraction discontinuity that represents a bubbly shock is seen in figure 13(*d*). The bubbly shock waves are characterized by the abrupt change in void fraction (β) values in a direction tangential to the suction-side surface of the hydrofoil, highlighted in figure 13(*d*). This bubbly shock wave causes the cavity to pinch-off and shed, as shown in figure 13(*e*,*f*).

Figure 14(*a*,*b*) shows the unsteady pressure $\mathrm{d}p_1$ observed in shedding cycles discussed in figures 12 and 13. For the re-entrant flow driven shedding cycle (figure 14*a*), $\mathrm{d}p_1$ reduces from (1) to (2) as the cavity begins to fill with vapour. As the cavity continues to grow and the re-entrant flow develops, $\mathrm{d}p_1$ does not register an increase in pressure between (2) and (4). From figure 12(*d*) it is seen that at this instance, when a layer of liquid covers

https://doi.org/10.1017/jfm.2022.999 Published online by Cambridge University Press

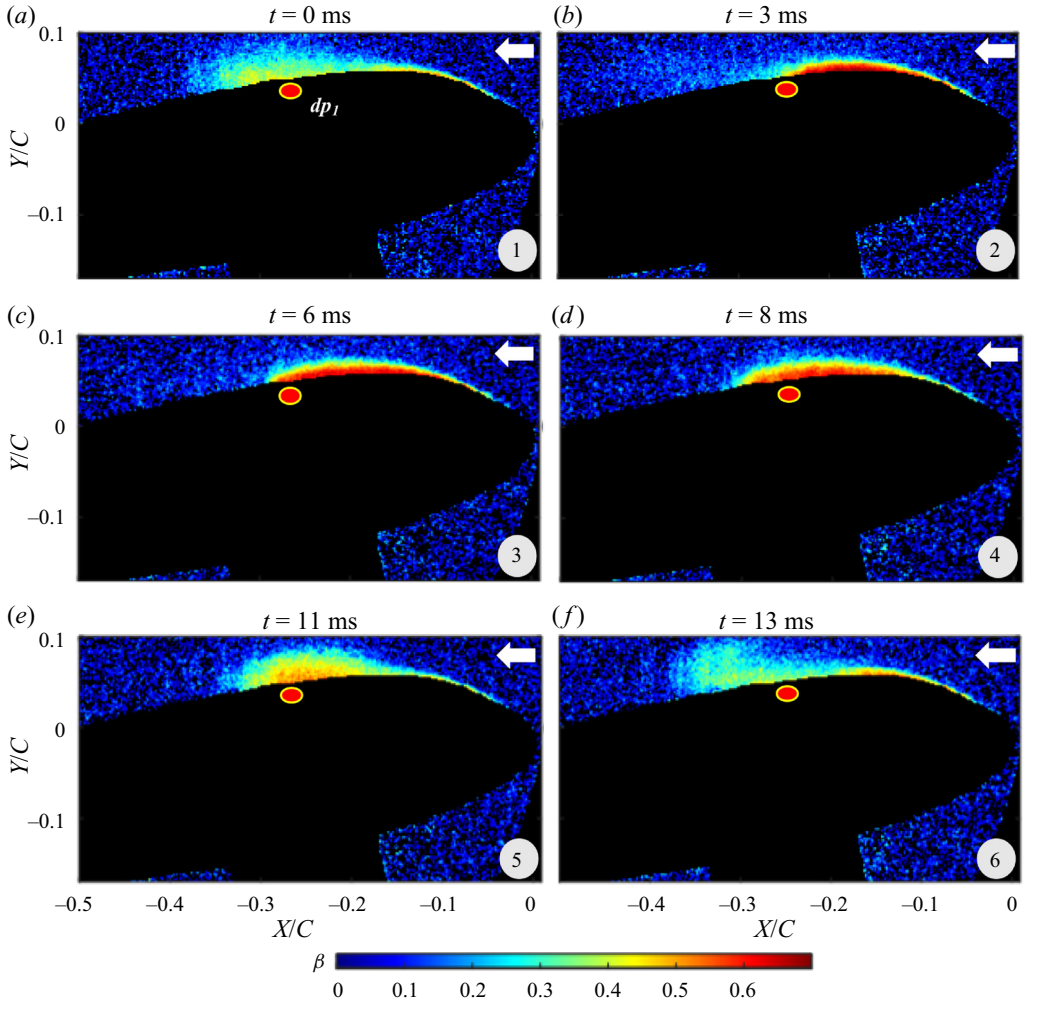

Figure 9. Time series of void fraction fields, β, from a stable partial type (i) cavity at $\sigma_0/2\alpha = 9.2$. The void fraction fields reveal a region of high void fraction near the surface, but the cavity thinness precludes the ability to observe thin near-surface liquid flow. (See supplementary movie 1 available at https://doi.org/10.1017/jfm.2022.999.)

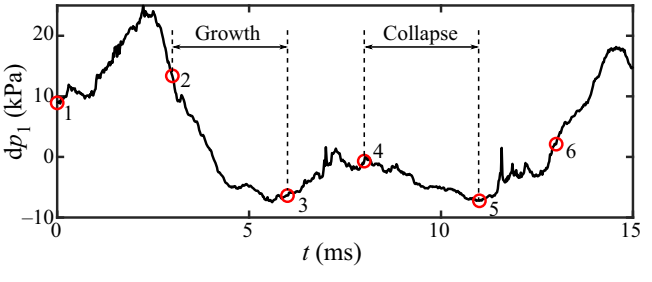

Figure 10. The surface pressure $\mathrm{d}p_1$ for a shedding cycle of a type (i) cavity that is likely driven by a re-entrant liquid flow at $\sigma_0 = 3.15$ ($\sigma_0/2\alpha = 9.04$). The cavity oscillates periodically, and the pressure $\mathrm{d}p_1$ drops when the surface of the transducer is covered with vapour.

https://doi.org/10.1017/jfm.2022.999 Published online by Cambridge University Press

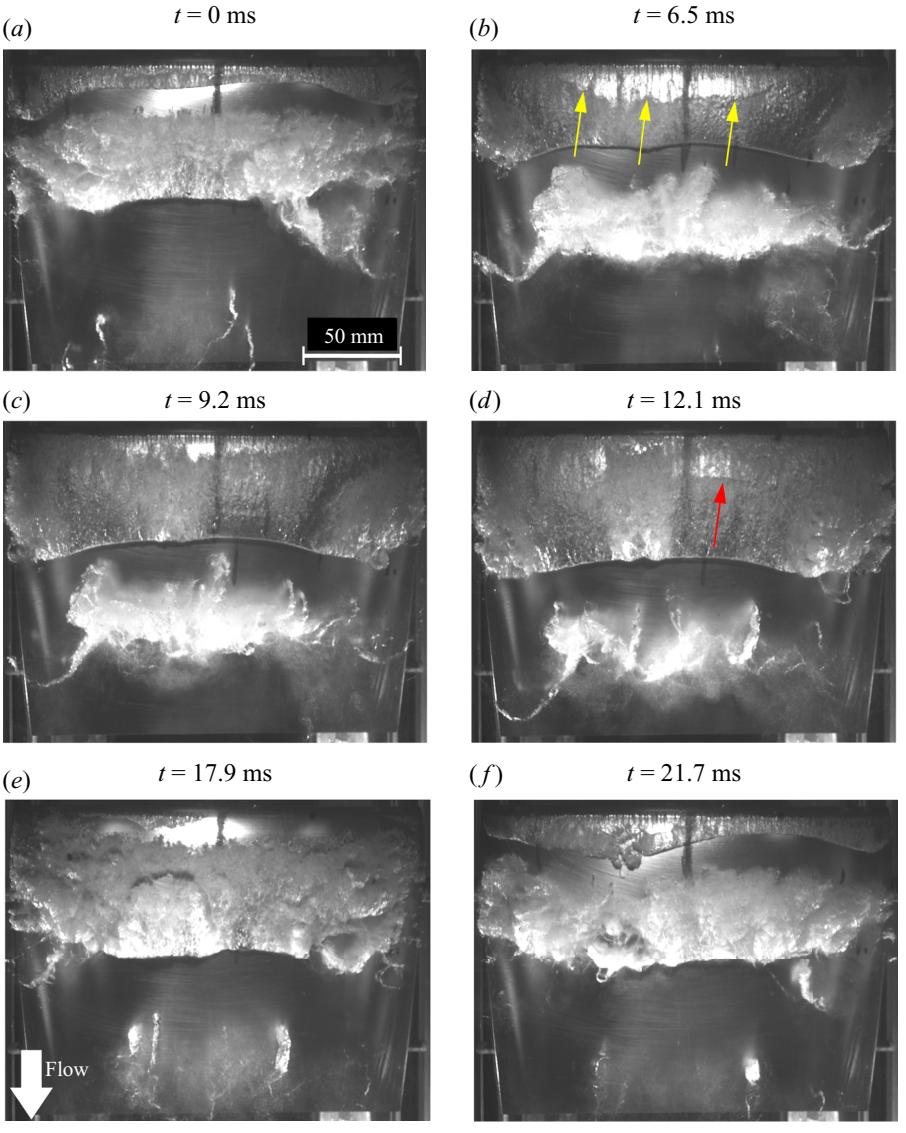

Figure 11. Images of a type (ii) partial cavity at $\sigma_0/2\alpha = 7.5$. Yellow and red arrows highlight the re-entrant liquid flow and a secondary flow front, respectively. The arrows highlight the flow fronts that lead to cavity pinch-off.

dp_1, no appreciable increase in pressure is registered by dp_1. Instead, dp_1 increases as the re-entrant liquid flow causes cavity pinch-off between figure 14(*a*)(4,5). This lack of pressure rise is important evidence that the observed flow structure is a liquid re-entrant flow and not a bubbly shock wave. A bubbly shock wave driven shedding cycle is shown in figure 13. When cavity growth begins, the pressure reduces from figure 14(*b*) (1) to (3), with a peak between (2) and (3). It is not clear what causes this peak, but it is likely due to the shed cloud collapse between (2) and (3), as shown in figure 13(*b*,*c*). The cavity collapse begins at (*d*) and the bubbly shock crosses dp_1 between (*d*) and (*e*), as seen in figure 13(*d*,*e*). Passage of the bubbly shock over dp_1 registers a pressure rise that is annotated in figure 14(*b*). This pressure rise is between 3–5 kPa depending on the shedding cycle.

https://doi.org/10.1017/jfm.2022.999 Published online by Cambridge University Press

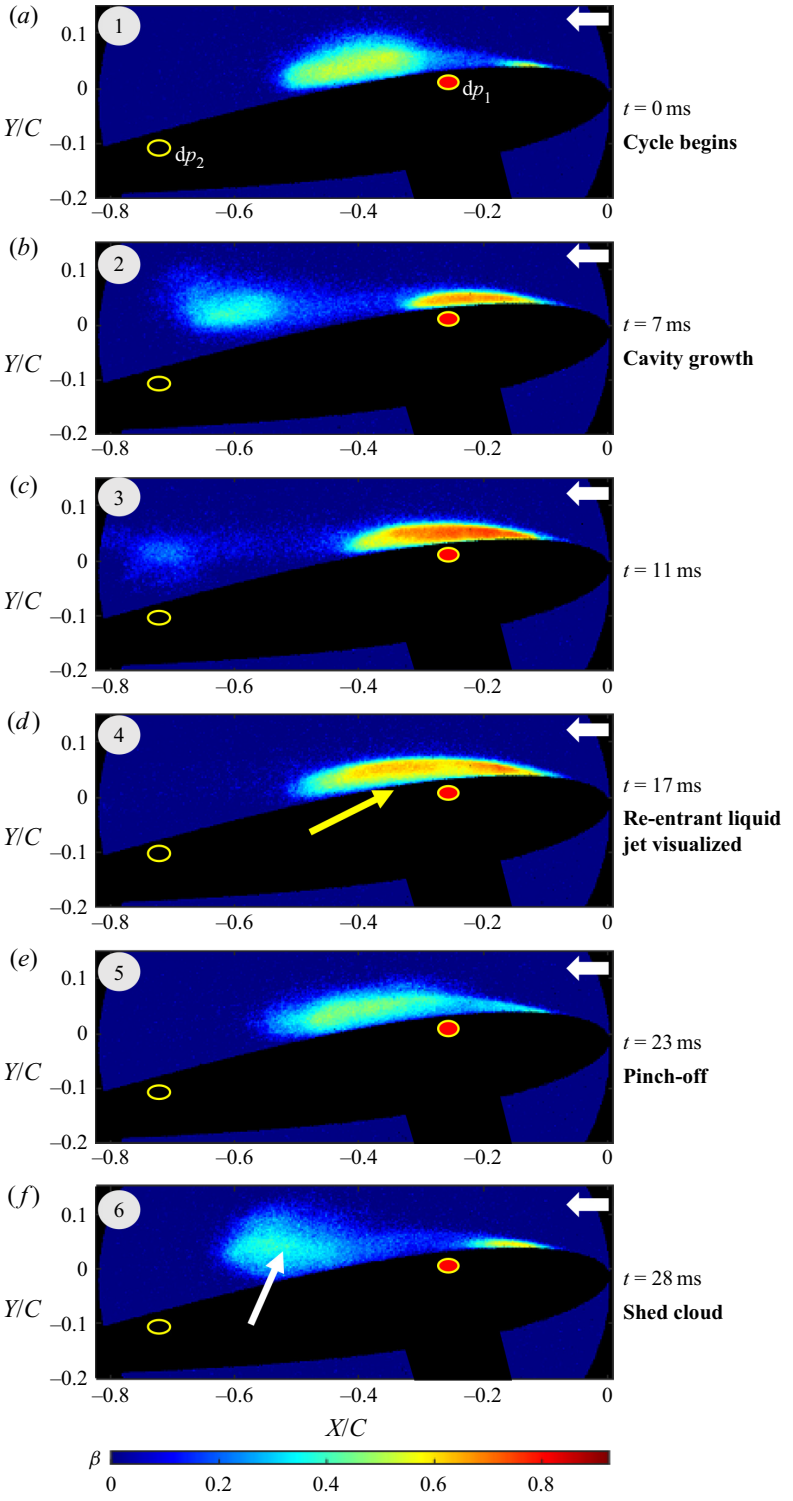

Figure 12. Time series of void fraction fields, β, from a shedding type (ii) cavity at $\sigma_0/2\alpha = 7.5$. The images illustrate a shedding cycle where re-entrant liquid flow causes cavity pinch-off. The location of the two surface pressure transducers are illustrated by the circles. (See supplementary movie 2.)

https://doi.org/10.1017/jfm.2022.999 Published online by Cambridge University Press

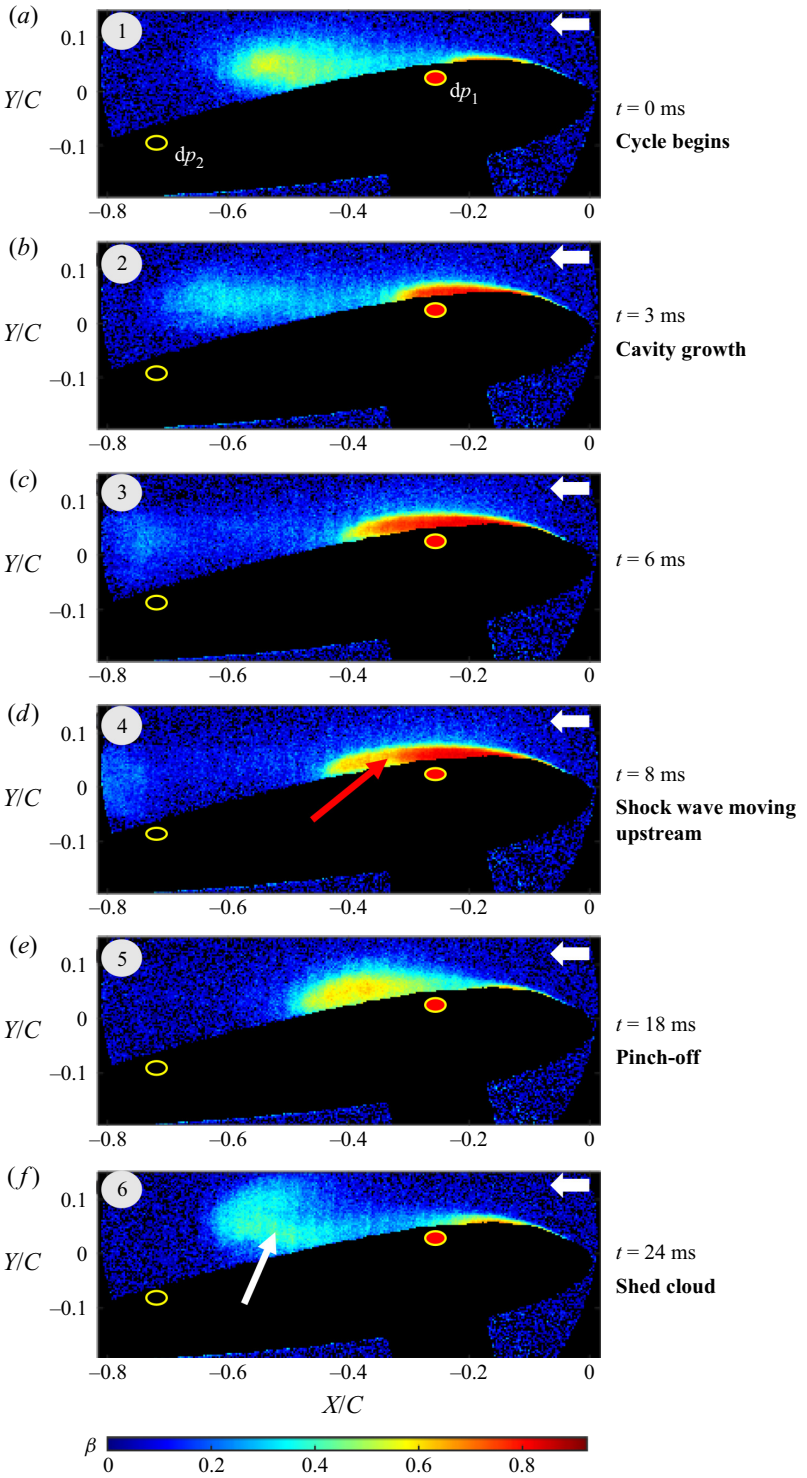

Figure 13. Time series of void fraction fields, β, from a cavity for type (ii) at $\sigma_0/2\alpha = 7.5$. The images illustrate a shedding cycle where the propagation of a bubbly shock front causes cavity pinch-off. The location of the two surface pressure transducers are illustrated by the circles. (See supplementary movie 2.)

https://doi.org/10.1017/jfm.2022.999 Published online by Cambridge University Press

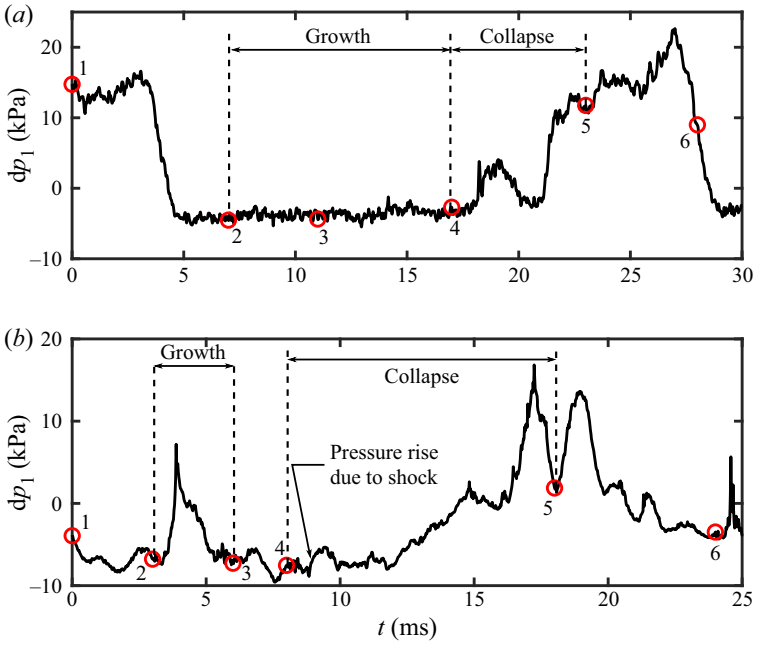

Figure 14. The surface pressures dp_1 for a shedding cycle of a type (ii) cavity at $\sigma_0/2\alpha = 7.5$) with (*a*) re-entrant liquid flow shedding shown in figure 12 and (*b*) shock wave driven shedding shown in figure 13.

6. Cavity with shedding caused by bubbly shocks: type (iii)

Type (iii) cavities appear for $6.1 > \sigma_0/2\alpha > 5.1$ with $0.6 < L_C/C < 0.85$. Cavity pinch-off is mostly caused by bubbly shock waves with re-entrant flows causing occasional cavity pinch-off. Figure 15 shows a time series of shedding observed for type (iii) cavity at $\sigma_0/2\alpha = 5.4$. The cycle begins with the cavity growth near the leading edge, as shown in figure 15(*a*). Upon attaining a length of about $0.4C$, a flow structure originates at the closure region of the growing cavity similar to the flow front seen in the closure region of type (i) and (ii) cavities (orange arrows in figure 15*b*,*c*). When the cavity attains its maximum length in a given cycle, another feature originates at the closure (red arrows in 15*d*,*e*). This structure propagates upstream, significantly faster than the previous structure, causing the cavity to be pinched-off from the leading edge, as shown in figure 15(*e*–*g*).

Figure 16 shows an X-ray densitometry based void fraction flow field for a type (iii) cavity experiencing bubbly shock-induced shedding. The cycle begins by cavity growth as shown in figure 16(*a*). The cavity continues to grow and attains a maximum length that extends beyond the X-ray field of view, as seen in figure 16(*b*–*d*). During this growth process, liquid accumulates underneath the cavity, with the liquid flow being thicker near cavity closure, as seen in figure 16(*b*–*d*). Figure 16(*d*) also shows a liquid re-entrant flow front near the cavity attachment point. This flow front is almost stationary and unable to cause cavity pinch-off. A bubbly shock causes the cavity to collapse near the cavity closure, travelling past the liquid re-entrant flow to cause pinch-off from the leading edge, as shown in figure 16(*e*–*i*).

Most of the shedding cycles observed for type (iii) cavities were caused by propagating bubbly shock waves (figure 16), with a liquid re-entrant flow co-existing underneath the cavity but unable to cause pinch-off. Despite the bubbly shock dominant shedding occurring for the majority of the shedding cycles, re-entrant liquid occasionally caused

https://doi.org/10.1017/jfm.2022.999 Published online by Cambridge University Press

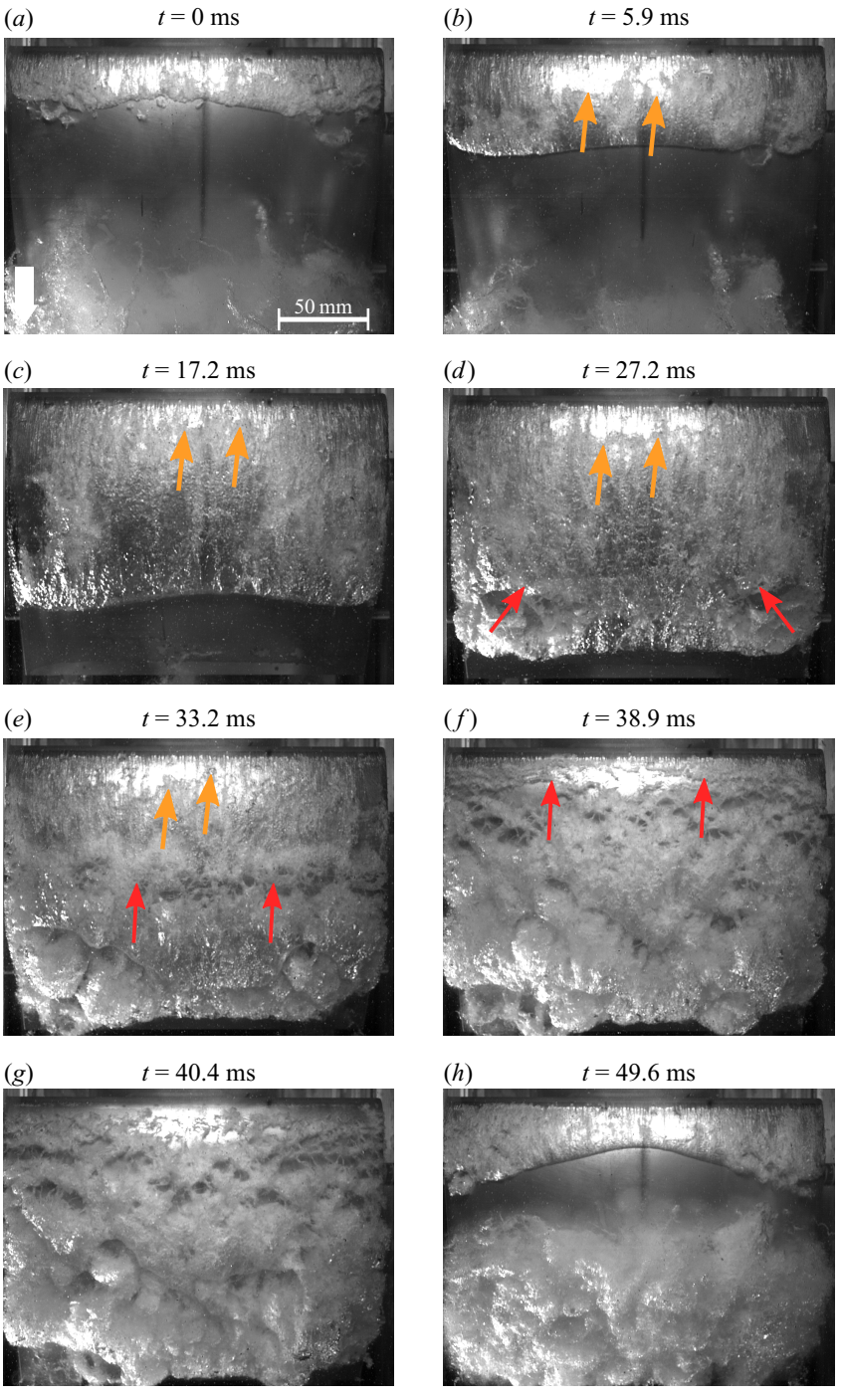

Figure 15. Images of a partial cavity for type (iii) at $\sigma_0/2\alpha = 5.4$ showing a representative type (iii) cavity. Two flow fronts are observed, with orange and red arrows highlighting each flow front. The flow front highlighted by orange arrows remains trapped underneath the cavity and the red arrow flow front ultimately leads to cavity pinch-off.

https://doi.org/10.1017/jfm.2022.999 Published online by Cambridge University Press

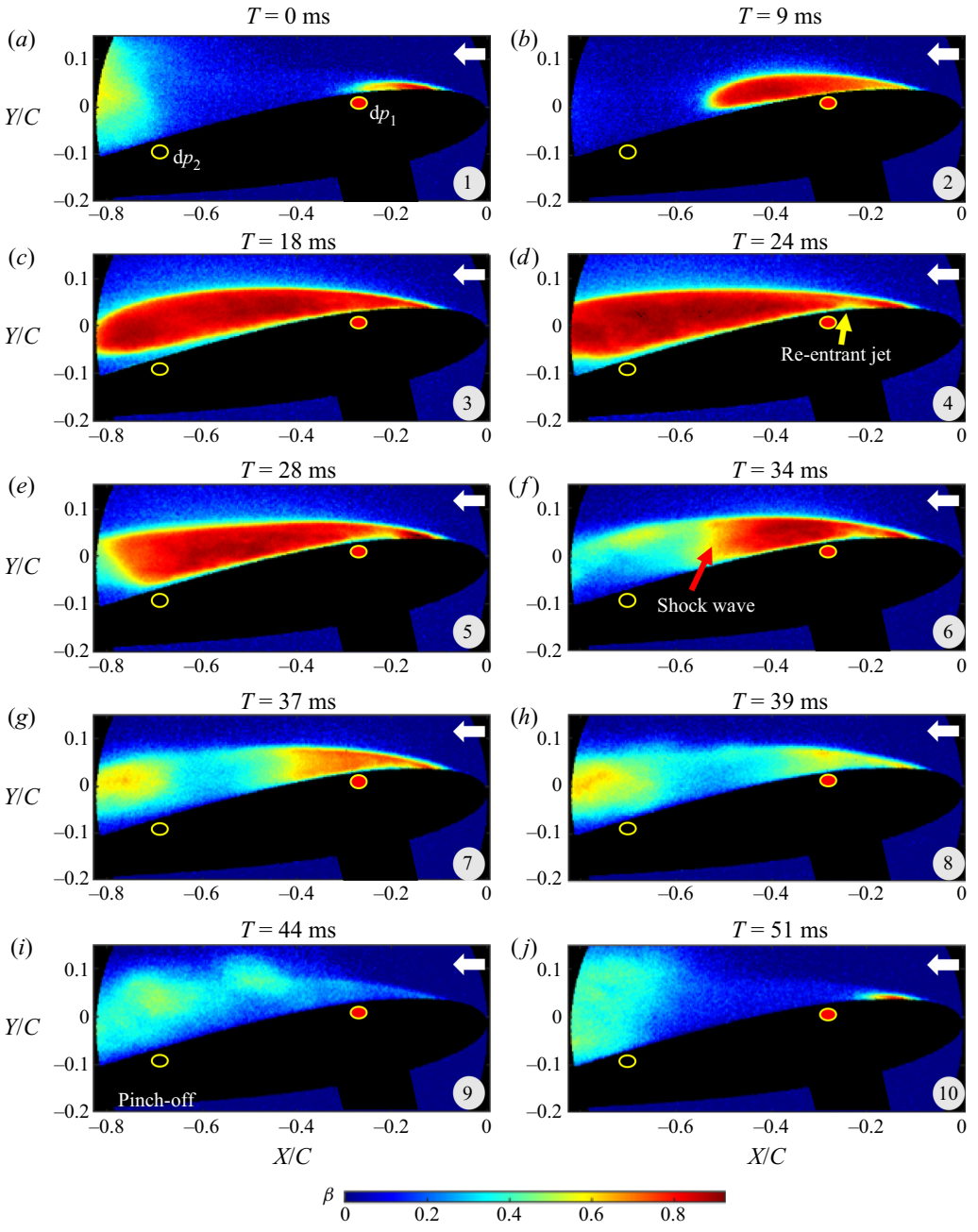

Figure 16. Time series of void fraction fields, β, for a type (iii) cavity at $\sigma_0/2\alpha = 5.4$. The images illustrate a shedding cycle where the propagation of a shock front causes cavity pinch-off. The location of the two surface pressure transducers are illustrated by the circles. From (4) to (7), the trapped re-entrant flow front is unable to cause pinch-off; (5)–(7) shows the advancing shock wave moving upstream to cause pinch-off near the leading edge. (See supplementary movie 3.)

https://doi.org/10.1017/jfm.2022.999 Published online by Cambridge University Press

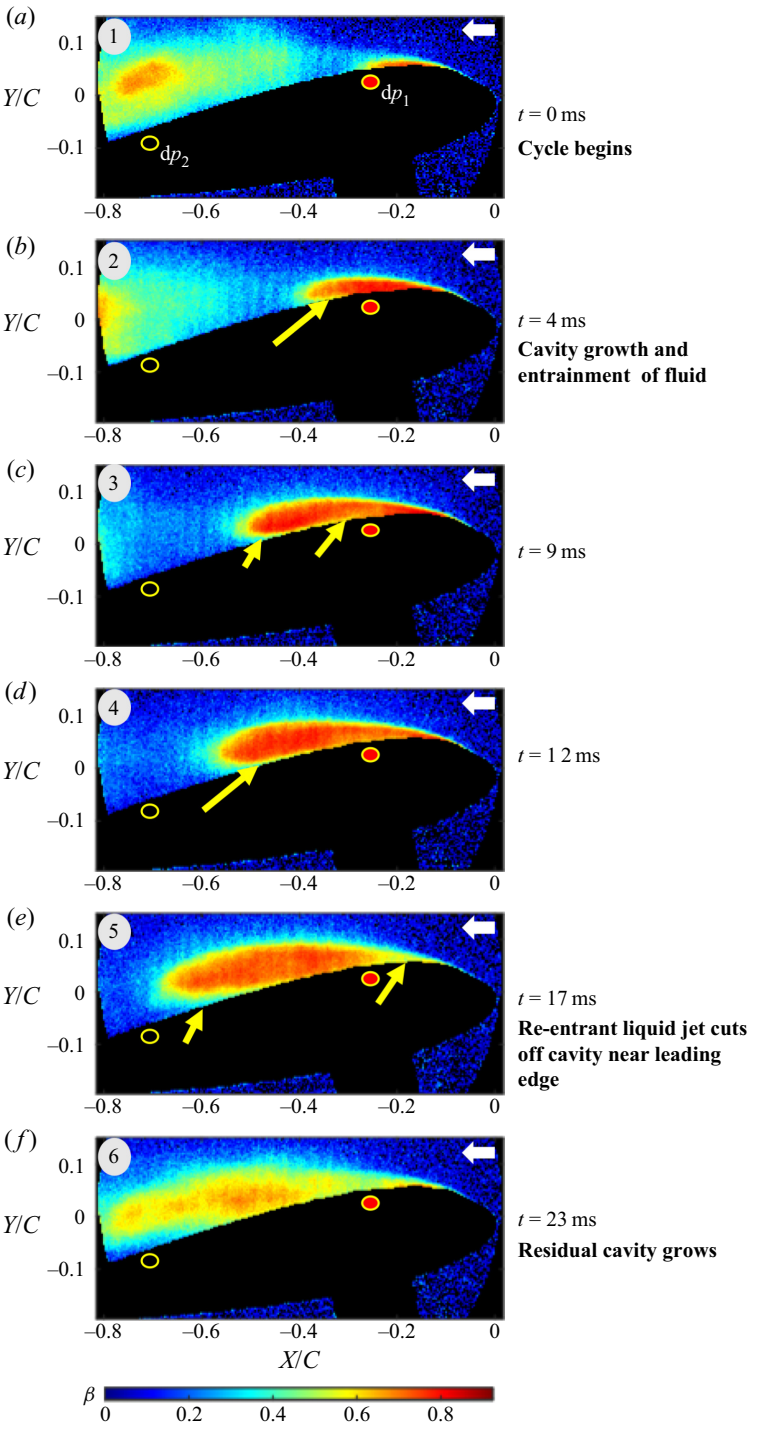

Figure 17. Time series of void fraction fields, β, from a type (iii) cavity at $\sigma_0/2\alpha = 5.4$. The images illustrate a shedding cycle where re-entrant liquid flow causes cavity pinch-off. The location of the two surface pressure transducers are illustrated by the circles. Despite the dominance of bubbly shock waves as a cavity pinch-off mechanism, the re-entrant liquid flow is sometimes observed to produce cavity pinch-off. (See supplementary movie 3.)

https://doi.org/10.1017/jfm.2022.999 Published online by Cambridge University Press

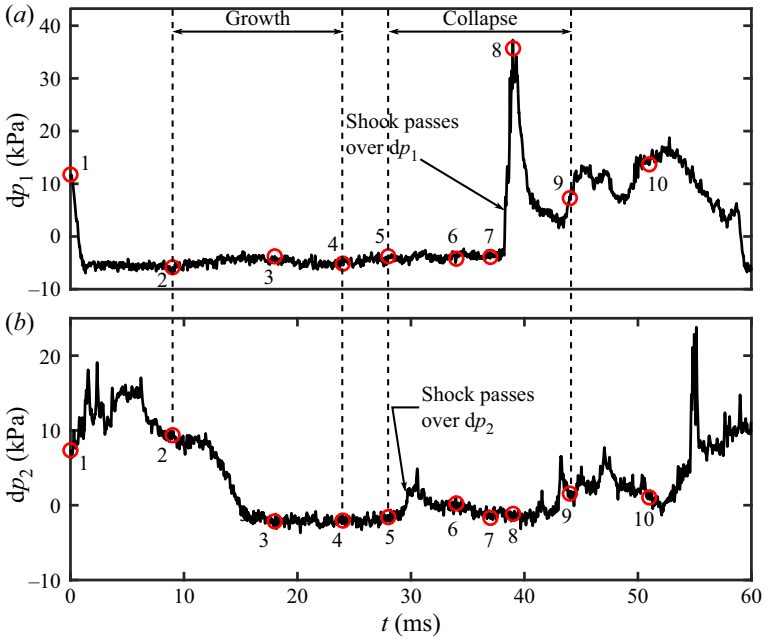

Figure 18. The surface pressures dp_1 (*a*) and dp_2 (*b*) for a shedding cycle of a type (iii) cavity at $\sigma_0/2\alpha = 5.4$ depicted in figure 16. From (4) to (7) the trapped re-entrant flow front does not significantly affect the unsteady surface pressure at dp_1. A 14.6 kPa pressure rise due to the shock wave front passing over dp_1 is highlighted between (7)–(8) in (*a*). Similarly, a 5.9 kPa pressure rise over dp_2 is highlighted between (5)–(6) in (*b*).

cavity pinch-off near the leading edge of the foil. This is quantitatively presented in figure 26, where despite the dominance of shock waves, re-entrant flow still causes pinch-off. One such cycle where re-entrant flow causes pinch-off is shown in figure 17. Figure 17(*a*,*b*) shows the growth and the formation of the liquid re-entrant flow. As the cavity continues to grow, liquid accumulates at the cavity closure due to flow turning and propagates upstream, as shown in figure 17(*c*,*d*). This liquid re-entrant flow caused the cavity to pinch-off, as seen in figure 17(*e*), and the pinch-off occurred while the cavity was still growing. The maximum cavity length for the re-entrant flow caused shedding was shorter than the maximum cavity length seen in bubbly shock caused shedding, and the residual cavity subsequently grows.

The corresponding unsteady pressure values, dp_1 and dp_2 for the shedding cycle depicted in figure 16, are shown in figure 18. During the cavity growth phase, vapour covers the surface of dp_1 and dp_2, and a pressure drop is recorded as shown in figure 18(*a*)(1,2) and (*b*)(2,3), respectively. Passage of the liquid re-entrant flow over dp_1 and dp_2 does not register a substantial pressure rise, as seen in figure 18(*a*)(3–7) and 18(*b*)(3–5). A pressure rise due to the passage of the bubbly shock over dp_2 is seen between 18(*b*)(5,6) and over dp_1 in figure 18(*a*)(7,8). As the cavity pinches off from the leading edge, a large spike in pressure is registered at dp_1 as the transducer gets exposed to ambient pressure.

7. Cavity with dynamics influenced by trailing edge cavitation: type (iv)

Type (iv) cavities appear for $\sigma_0/2\alpha < 5.1$ with $L_C/C > 0.85$. Cavity shedding is caused mostly by bubbly shocks, but the influence of trailing edge cavitation is now present. Figure 19 shows snapshots in the form of a time series, depicting shedding observed for

https://doi.org/10.1017/jfm.2022.999 Published online by Cambridge University Press

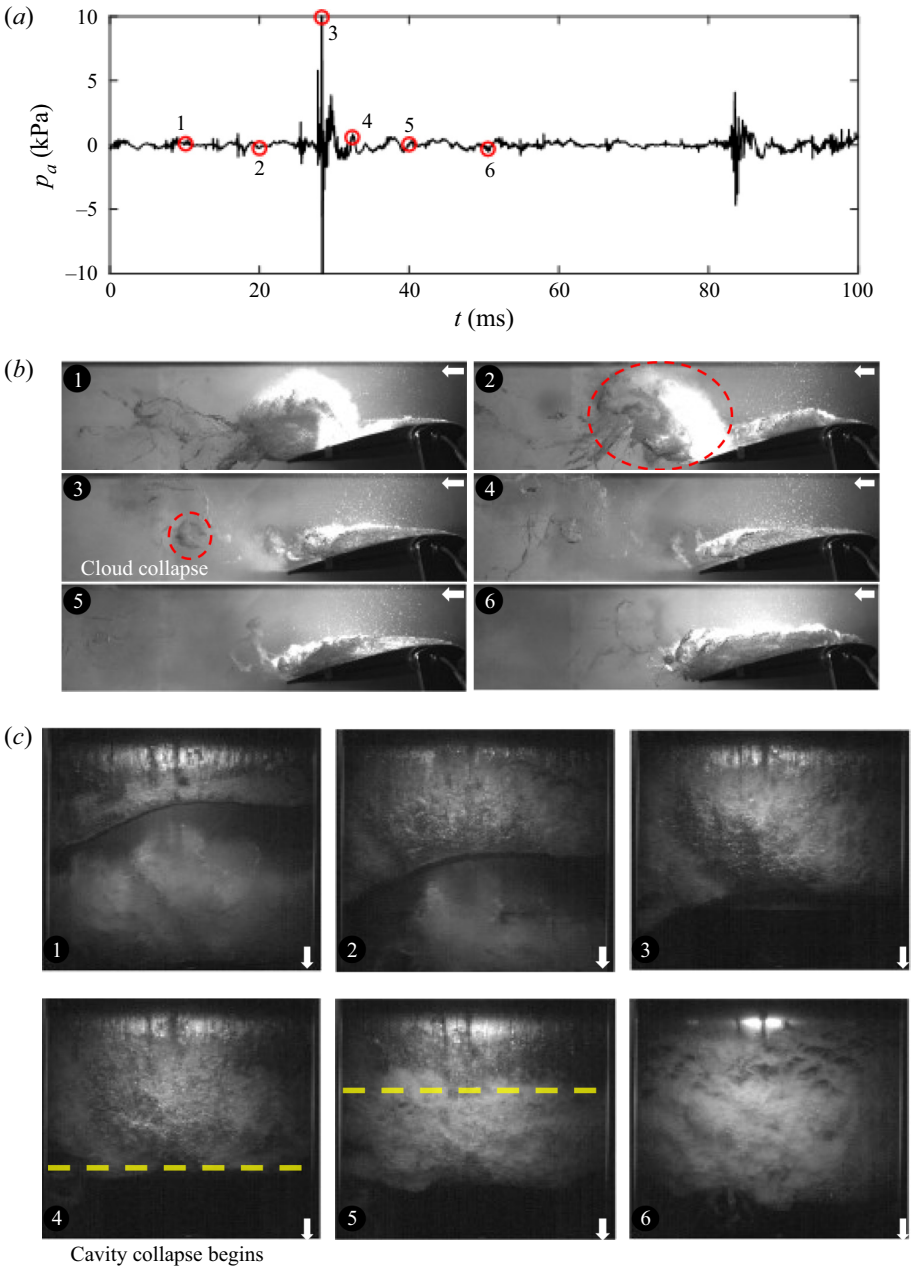

Figure 19. A time series of high-speed images for type (iv) at $\sigma_0/2\alpha = 4.1$ that highlights the collapse of a shed vapour cloud downstream of the hydrofoil that then initiates the collapse of the subsequent attached cavity. The hydrophone signal (*a*) records the acoustic pressure, p_a, that is correlated with the images before and after cloud collapse. The corresponding side-view (*b*) and top-view (*c*) images show the cloud collapse process. (See supplementary movie 6.)

a type (iv) cavity at $\sigma_0/2\alpha = 4.1$. Here, there is significant cavitation near the trailing edge that interacts with the main cavity forming on the suction side. The rotation of the shed trailing edge cavitation cloud is opposite signed compared with the rotation of the shed cloud from the main cavity over the hydrofoil as seen in Figure 1. Figure 19 shows a

https://doi.org/10.1017/jfm.2022.999 Published online by Cambridge University Press

type (iv) shedding cycle synchronous with acoustic pressure measurements p_a, where p_a is the signal detected by a hydrophone mounted in a liquid pocket located on the top of the tunnel wall 0.25 C away from the trailing edge of the hydrofoil. As the main cavity attains maximum length, the shed cloud from the previous shedding cycle collapses near the trailing edge, as shown in figure 19(*a*)(3). This collapse causes a pressure pulse that is recorded as a 12 kPa impulse by the hydrophone. After this pressure pulse, the suction-side cavity begins to collapse between (4)–(6), as seen in top-view snapshots in figure 19(*c*). This illustrates how the collapse of the convecting vapour cloud initiates the following cavity collapse process for a type (iv) cavity.

The void fraction time series depicting shedding dynamics of a type (iv) cavity is shown in figure 20. The cycle begins with cavity growth from the leading edge of the hydrofoil as seen in figure 20(*a*,*b*). As the cavity grows, liquid re-entrant flow begins to develop at the cavity closure, as seen in figure 20(*c*,*d*), and it travels upstream as seen in figure 20(*e*–*g*). However, the cavity collapse is caused by a bubbly shock propagating toward the leading edge, as seen in figure 20(*e*–*h*), followed by pinch-off as shown in figure 20(*i*). The shedding mechanisms observed for type (iv) cavities are similar to type (iii), and both the re-entrant flow and bubbly shock waves are present. Cavity pinch-off was dominated by the propagation of bubbly shock waves and rarely by liquid re-entrant flow. As seen in type (iii) cavities, re-entrant flow can occasionally lead to cavity pinch-off, as shown in figure 21. The re-entrant flow is seen to approach the leading edge from (*c*)–(*e*) and cut off the cavity near the leading edge at (*f*). The residual cavity then grows and a normal shedding cycle resumes.

To visualize cavitation near the trailing edge the field of view of the densitometry system was moved downstream. A time series of instantaneous void fraction measurements for type (iv) cavitation near the trailing edge is shown in figure 22. The cycle starts with the pinch-off of the main cavity on the surface of the hydrofoil caused by a bubbly shock, as shown in figure 22(*a*). As the bubbly shock travels upstream, vapour is shed from the interface and this shed vapour cloud is seen near the trailing edge in figure 22(*b*,*c*). Meanwhile, cavitation occurs at the trailing edge on the suction side and begins to interact with the shed cloud in figure 22(*c*,*d*) forming lobe 1. As the shed vapour from the main cavity moves downstream, it interacts with lobe 1, causing formation of lobe 2 in figure 22(*f*,*g*). Lobe 2 interacts with lobe 1 in figure 22(*g*–*i*) and a cloud is shed from the trailing edge in figure 22(*j*). The presence of a long and thick cavity on the hydrofoil, as observed in type (iv), is similar to open cavities observed in wakes, as discussed in Wu *et al.* (2021). The thick cavity shed from the suction side and the trailing edge are counter-rotating, resembling spanwise vortices in the near-wake region of a bluff body. They interact in a manner similar to the two counter-rotating spanwise vortices observed in the cavitating wakes of two-dimensional bluff bodies (Wu *et al.* 2021).

8. Re-entrant flow and bubbly shock properties

Re-entrant flow thickness was estimated using high-speed images. When re-entrant liquid flows were observed, the thickness of the re-entrant flow, t_J, at 85 % of L_C is typically 0.3 to 3.2 mm or roughly 5 % to 15 % of the maximum cavity thickness, t_C, as shown in figure 23. Observed re-entrant flow thickness in the present study is less than half the typical value reported by Callenaere *et al.* (2001) for a cloud shedding cavity formed behind a backward facing step (15 % to 35 % of the maximum cavity thickness). The re-entrant flow convects upstream from the closure region of the cavity and can cause the cavity to separate when

https://doi.org/10.1017/jfm.2022.999 Published online by Cambridge University Press

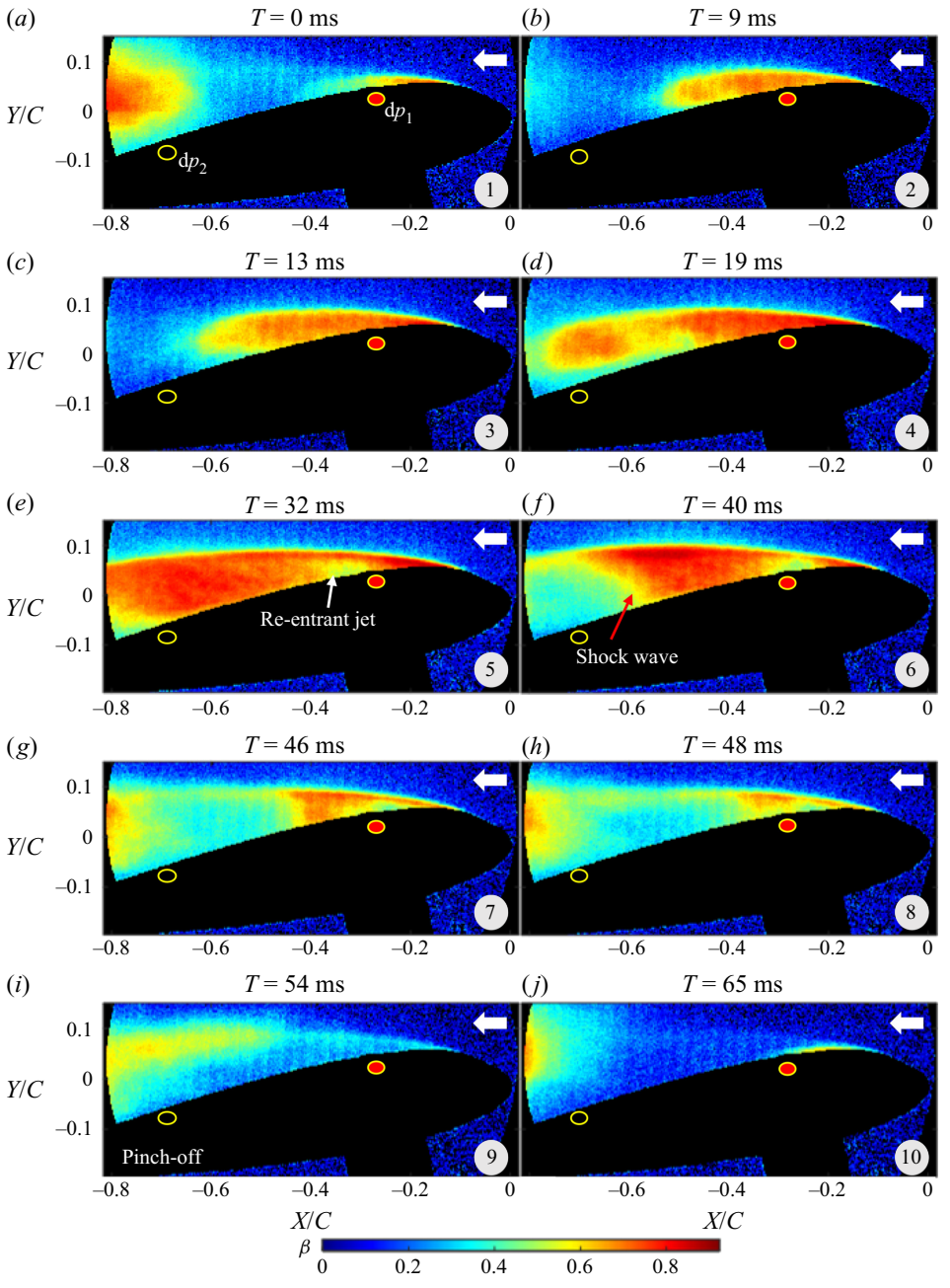

Figure 20. Time series of void fraction fields, β, for a type (iv) cavity at $\sigma_0/2\alpha = 4.1$. The location of the two surface pressure transducers are illustrated by the circles. A bubbly shock causes the cavity pinch-off, although re-entrant liquid flow can also be observed. (See supplementary movie 4.)

it impinges near the hydrofoil leading edge. The average re-entrant flow speed estimated from void fraction fields is between 3 and 6 m s^{-1}, or roughly 41–75 % of the free-stream speed. This range is consistent with the observations reported by Callenaere *et al.* (2001).

https://doi.org/10.1017/jfm.2022.999 Published online by Cambridge University Press

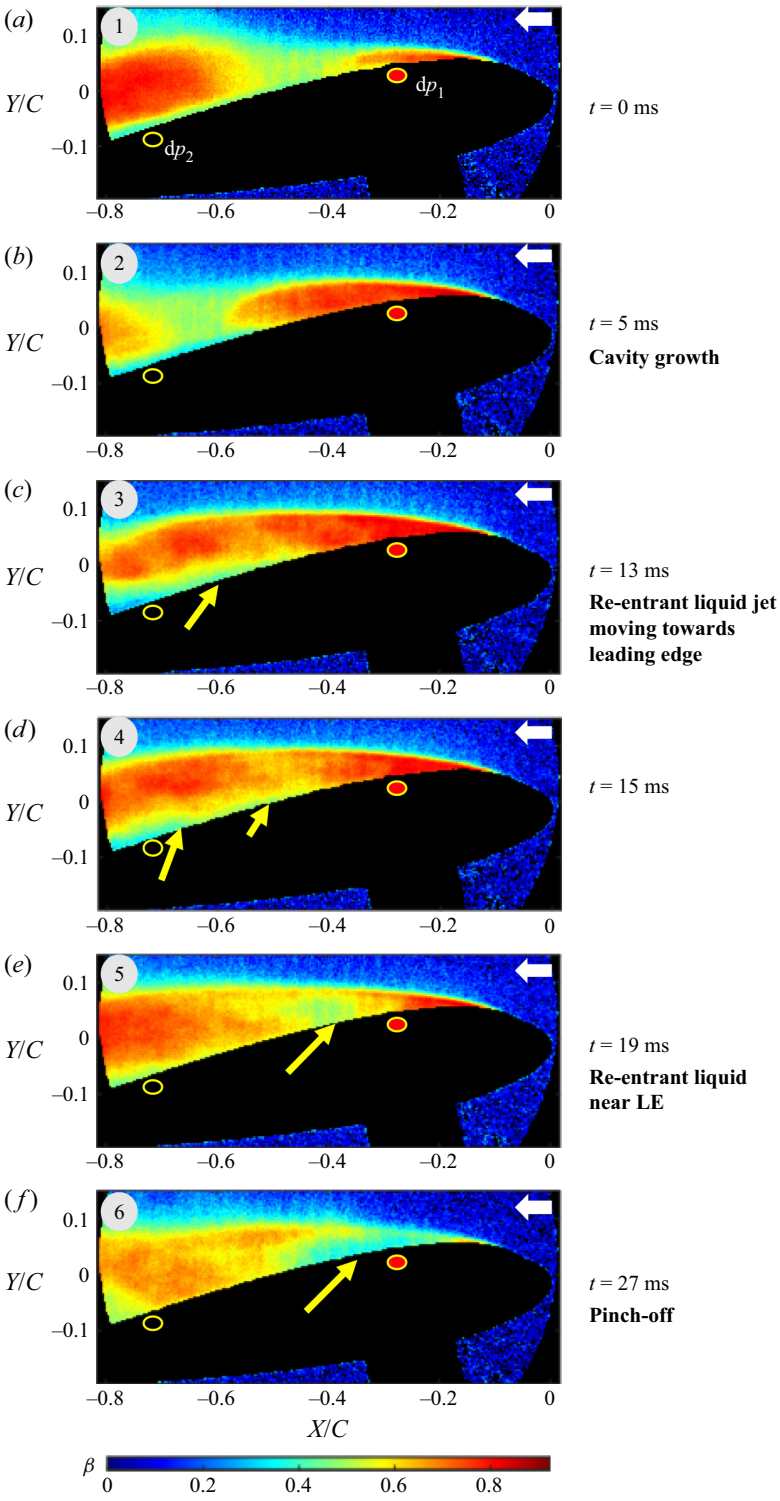

Figure 21. Time series of void fraction fields, β, from a type (iv) shedding cavity at $\sigma_0/2\alpha = 4.1$, where liquid re-entrant flow causes cavity pinch-off near the leading edge. (See supplementary movie 4.)

https://doi.org/10.1017/jfm.2022.999 Published online by Cambridge University Press

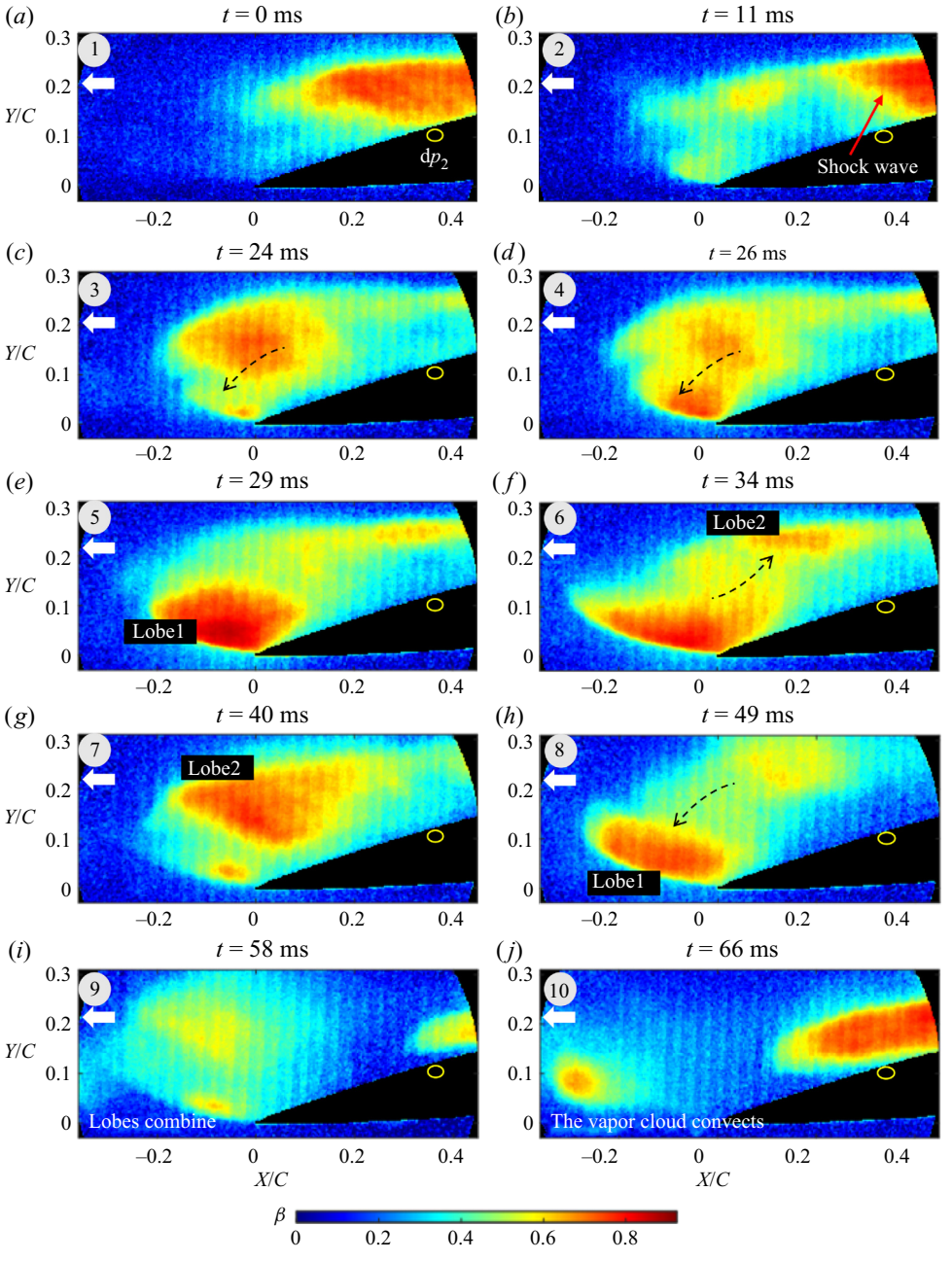

Figure 22. Time series of void fraction fields, β, for a type (iv) at $\sigma_0/2\alpha = 4.1$. The field of view is moved downstream to show the trailing edge. The location of the aft surface pressure transducers is illustrated by the circle. The cavity shed from the suction side and the trailing edge cavity interact, and this interaction is similar to that between two counter-rotating regions of cavitating flow observed in wakes of bluff objects, as discussed by Wu *et al.* (2021). (See supplementary movie 5.)

https://doi.org/10.1017/jfm.2022.999 Published online by Cambridge University Press

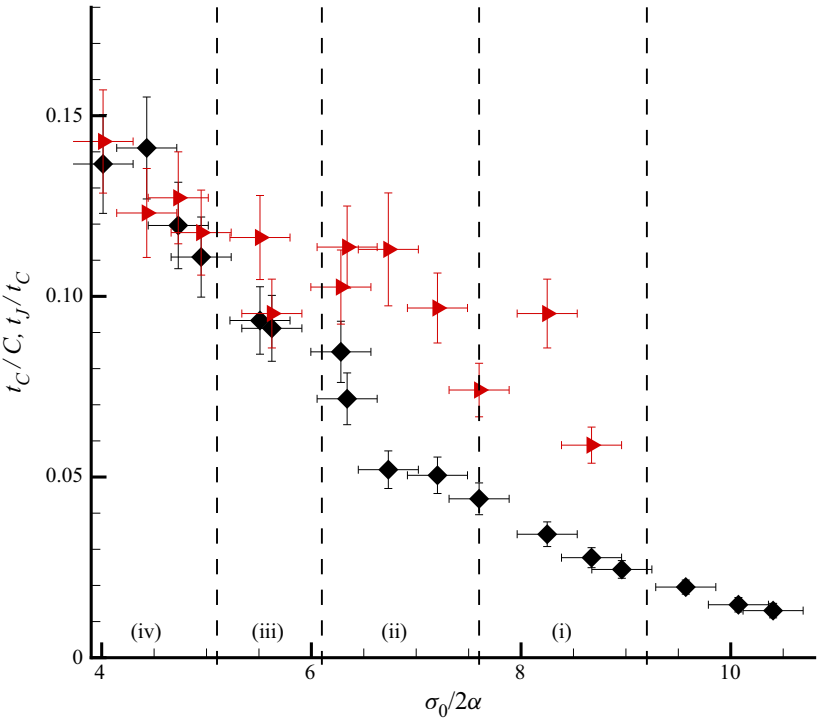

Figure 23. Maximum cavity thickness, t_C/C (♦), and re-entrant flow thickness, t_J/t_C (red triangle right), varying with $\sigma_0/2\alpha$.

For cavities with bubbly shock waves, we can measure the shock speed directly from the examination of $s-t$ diagrams of near-surface void fraction, as discussed by Ganesh *et al.* (2016) and Bhatt *et al.* (2021). The $s-t$ diagrams trace the change in void fraction values along the tangential curve 's' on the suction side of the hydrofoil, as shown in figure 24, with time. In addition, the shock speed can be independently estimated using conservation of mass and momentum across a normal shock interface. Assuming negligible heat transfer and neglecting bubble dynamics, the expression for shock propagation speed, u_S, can be obtained by using (Brennen 2005),

$$u_S^2 = \frac{(p_2 - p_1)}{\rho_L}\left[\frac{(1-\beta_2)}{(1-\beta_1)(\beta_1-\beta_2)}\right], \tag{8.1}$$

where β_1 and β_2 are the void fraction values upstream and downstream of the front, and $p_2 - p_1$ is the pressure rise across the front. The void fraction is measured from the X-ray measurements, and the pressure rise is determined from the unsteady surface pressure measurements as the front passes over the transducer. The direct measurement of u_S is made in the laboratory frame using the $s-t$ diagram generated along the curve parallel to the surface of the hydrofoil, as shown in figure 24. Figure 25 presents the directly measured and the computed shock speed normalized by the upstream flow speed, u_S/u_0. The speed computed using (8.1) is consistent with the speed that was directly measured. This implies that the jump conditions adequately captures the mass and momentum conservation across the shock front, and that velocity of the bubbly mixture within the cavity is much slower (e.g. closer to zero speed) than the shock speed as it convects upstream. The shock

https://doi.org/10.1017/jfm.2022.999 Published online by Cambridge University Press

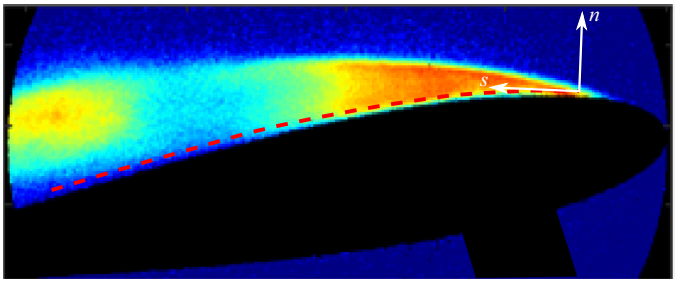

Figure 24. Schematic depicting the tangential direction (s) and normal direction (n) to the surface of the hydrofoil. The $s-t$ diagrams are made using the curve (red dashed line) and u_S is measured directly.

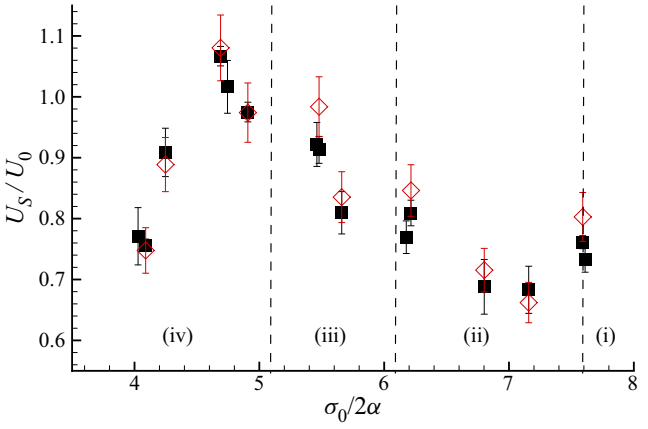

Figure 25. The shock speed u_S/u_0 for varying of $\sigma_0/2\alpha$. The speed was directly measured in the laboratory frame (■) and computed using (8.1) (red diamond) for hydrofoil at $\alpha = 10^\circ$.

speed peaks for type (iv) cavities, which also are dominated by shock-induced shedding processes.

9. Probability that re-entrant flows or bubbly shock waves will lead to cavity pinch-off

The results presented above illustrate that cavity pinch-off can be caused by both re-entrant flows and bubbly shocks. With changing $\sigma_0/2\alpha$, we see that the likelihood of pinch-off caused by either cavity shedding mechanism changes. In this section the probability of cavity pinch-off caused by re-entrant flows and bubbly shock waves is estimated. We define the event probability as the probability of cavity shedding caused by a particular mechanism as determined from time-resolved void fraction measurements. The probability definitions are shown in (9.1) and (9.2), where N_R, N_S are the number of re-entrant flow driven shedding cycles and shock wave driven shedding cycles, respectively, for N total cycles,

$$P_R = \frac{N_R}{N}, \tag{9.1}$$

$$P_S = \frac{N_S}{N}. \tag{9.2}$$

https://doi.org/10.1017/jfm.2022.999 Published online by Cambridge University Press

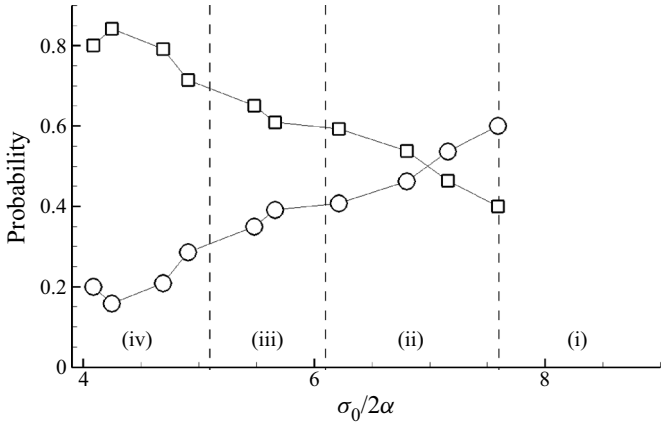

Figure 26. Event probability plot showing the probability of re-entrant flow causing cavity pinch-off, P_R (◯), along with bubbly shock waves causing pinch-off, P_S (□), as a function of $\sigma_0/2\alpha$. For longer type (iii) and type (iv) cavities, shock waves are the dominant mechanism of shedding, but re-entrant liquid jets can still cause cavity detachment.

Figure 26 shows the probability of liquid re-entrant flow and bubbly shock waves to cause cavity pinch-off for a given $\sigma_0/2\alpha$ at $\alpha = 10^\circ$. As $\sigma_0/2\alpha$ is reduced, the likelihood of pinch-off caused by bubbly shock increases and the likelihood of pinch-off caused by re-entrant flows decreases. The dominance of each flow front in different cavity shedding regimes can also be seen as $\sigma_0/2\alpha$ is reduced. We next consider the relationship between Mach number within the partial cavity and the likelihood of bubbly shock formation.

Previous studies such as Ganesh *et al.* (2016), Budich *et al.* (2018), Bhatt & Mahesh (2020), Wu *et al.* (2021) and Bhatt *et al.* (2021) have reported on the effect of mixture compressibility on the dynamics of high void fraction cavitating flows. At void fraction values $\beta > 0.1$, the speed of sound of the bubbly mixtures rapidly reduces and reaches a minimum around $\beta \approx 0.5$ (Brennen 2005). The sound speed of a cavitating bubbly mixture can be on the same order or slower than the speed of the surrounding liquid flow, making it locally supersonic and susceptible to the occurrence of bubbly shocks. By estimating the local speed of sound of the bubbly mixture within the separated region of the partial cavity, a Mach number based on the relevant velocity scales can be defined. The relationship between the likelihood of a given shedding mechanism and the estimated Mach number can then be sought.

The local speed of sound can be estimated by using a simplified expression for a homogeneous vapour–liquid mixture (Brennen 2005). Bhatt *et al.* (2021) demonstrated that the simplified speed of sound expression for a bubbly mixture is able to predict the onset of bubbly shock waves in shedding partial cavities behind a backward facing step. The general expression for the mixture sound speed is based on the assumption that the homogeneously dispersed vapour phase (subscript V) and the carrier liquid (subscript L) have no relative motion with negligible surface tension effects. Here, ϵ_L (ϵ_V) is the fraction of the liquid (vapour) phase in thermodynamic equilibrium with the vapour (liquid) phase. The general expression for the mixture speed of sound, c, is given by

$$\frac{1}{\rho_m c^2} = \frac{\beta}{p}[(1-\epsilon_V)f_V + \epsilon_V g_V] + \frac{1-\beta}{p^{1+\eta}}\epsilon_L g^* p_{cr}^{\eta}, \tag{9.3}$$

https://doi.org/10.1017/jfm.2022.999 Published online by Cambridge University Press

where β is the mixture void fraction, $\rho_m = \beta\rho_V + (1-\beta)\rho_L$ is the mixture density and p is the mixture pressure. For water, $g^* = 1.67$, $\eta = 0.73$, $g_V = 0.91$, $f_V = 0.73$ and $p_{cr} = 22.06$ MPa (Brennen 2005). For a general two component system with no inherent assumptions, g^*, η, g_V and f_V are thermodynamic functions encapsulating latent heat and temperature. We can make two bounding assumptions for heat transfer during phase change to develop the 'homogeneous equilibrium model' and the 'homogeneous frozen model.' The equilibrium model assumes instantaneous heat transfer between phases with $\epsilon_V = \epsilon_L = 0$, while the frozen model assumes zero heat transfer between phases with $\epsilon_V = \epsilon_L = 1$. The sound speed of a real two-phase mixture may lie somewhere between these bounds (Budich *et al.* 2018).

Bhatt *et al.* (2021) studied the validity of sound speed expressions based on the homogeneous frozen model and the homogeneous equilibrium model in predicting the experimental onset of bubbly shocks. They observed that the Mach number defined based on the velocity at the point of separation of the step and sound speed based on the homogeneous frozen model exhibited a subsonic to supersonic transition that coincided with the experimental observations of bubbly shocks. This result was contrasted with the Mach number based on the same velocity scale and sound speed based on the homogeneous equilibrium model, where the predicted Mach number was two orders of magnitude higher and, hence, always supersonic. Based on these findings, we will use the frozen model to estimate the local speed of sound (and Mach number) in the bubbly mixture within the cavity of the NACA0015 hydrofoil.

To evaluate the minimum sound speed based on (9.3), we need to determine the mixture pressure when the cavity is filled with vapour. The average static pressure within the cavity, p_c, was measured at the location depicted in figure 4(*a*), and this value represents the static pressure averaged over the entire shedding cycle. This includes conditions when the cavity mixture covers the pressure port as well as when the liquid flow is present over the measurement location. To determine the cavity pressure when the transducer is covered with vapour, we combine the average pressure value with time-synchronized surface pressure data from the unsteady pressure transducer, $\mathrm{d}p_1$, recorded at the same downstream location. As shown in the previous section, the dynamic pressure signal is correlated with various steps of the shedding cycle. The pressure change registered by $\mathrm{d}p_1$ can be subtracted from the mean pressure within the cavity to estimate static pressure at the time of shock propagation. This pressure is defined as p_S, such that $p_S = p_c - p^*$, where p^* is the pressure rise recorded by $\mathrm{d}p_1$ immediately after passage of the bubbly shock. Based on these static pressures, we can define a pressure coefficient, C_p as

$$C_p = \frac{p - p_0}{\frac{1}{2}\rho u_0^2}, \tag{9.4}$$

where p is a pressure of interest (p_c, p_S). The respective pressure coefficients (C_{p_c}, C_{p_S}) are shown in figure 27.

We can determine the mixture sound speed, c, based on p_S and corresponding void fraction measurement. The Mach number M_0 is defined based on 'c' and inflow velocity u_0 as

$$M_0 = \frac{u_0}{c}. \tag{9.5}$$

For every instantaneous void fraction flow field, a spatially varying Mach number field based on the cavity pressure p_S can be estimated. From this field we can then estimate the maximum cavity Mach number, M_{0P}, that corresponds to the condition of maximum cavity void fraction and minimum static pressure. Figure 28 shows the variation of M_{0P}

https://doi.org/10.1017/jfm.2022.999 Published online by Cambridge University Press

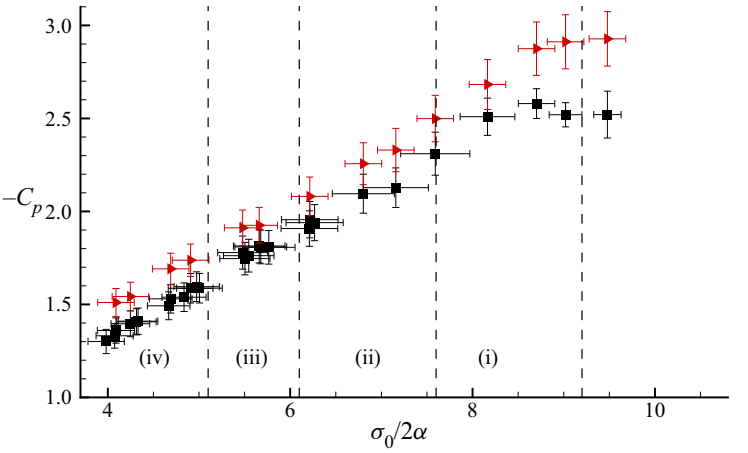

Figure 27. The pressure coefficients $-C_{pc}$ (■) and $-C_{ps}$ (red triangle right) varying with $\sigma_0/2\alpha$ for the foil at $\alpha = 10°$.

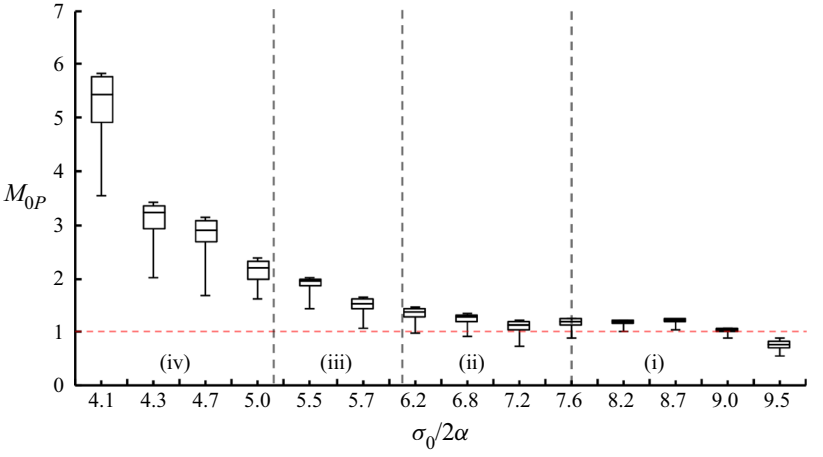

Figure 28. Box plot depicting variation of the peak value of M_{0P} that occurs over one shedding cycle with decreasing $\sigma_0/2\alpha$ across the different cavitation regimes. The boxes represent the median, the 75th and 25th percentiles. The whiskers represent the maximum and minimum values.

with $\sigma_0/2\alpha$ as a box plot. The boxes represent the median, the 75th and 25th percentiles. The whiskers represent the maximum and minimum values. The data in figure 28 reveals that the onset of bubbly shock waves coincides with the transition of the peak value M_{0P} from subsonic to supersonic. For type (iii) and (iv) cavities, $M_{0P} > 1$, both the upper and lower whiskers lie above unity. For type (ii) cavities, it is likely that $M_{0P} > 1$ for many cycles, and for type (i) cavities, there are conditions where the local Mach number does not reach unity. The median value of M_{0P} increases with decreasing $\sigma_0/2\alpha$ in tandem with the increasing likelihood of shock formation, as shown in figure 26.

We can also define a Mach number, M_S, using the local sound speed derived from the pressure within the cavity at the time of shock propagation, c, and shock speed, u_S, presented in figure 25 as

$$M_S = \frac{u_S}{c}, \tag{9.6}$$

https://doi.org/10.1017/jfm.2022.999 Published online by Cambridge University Press

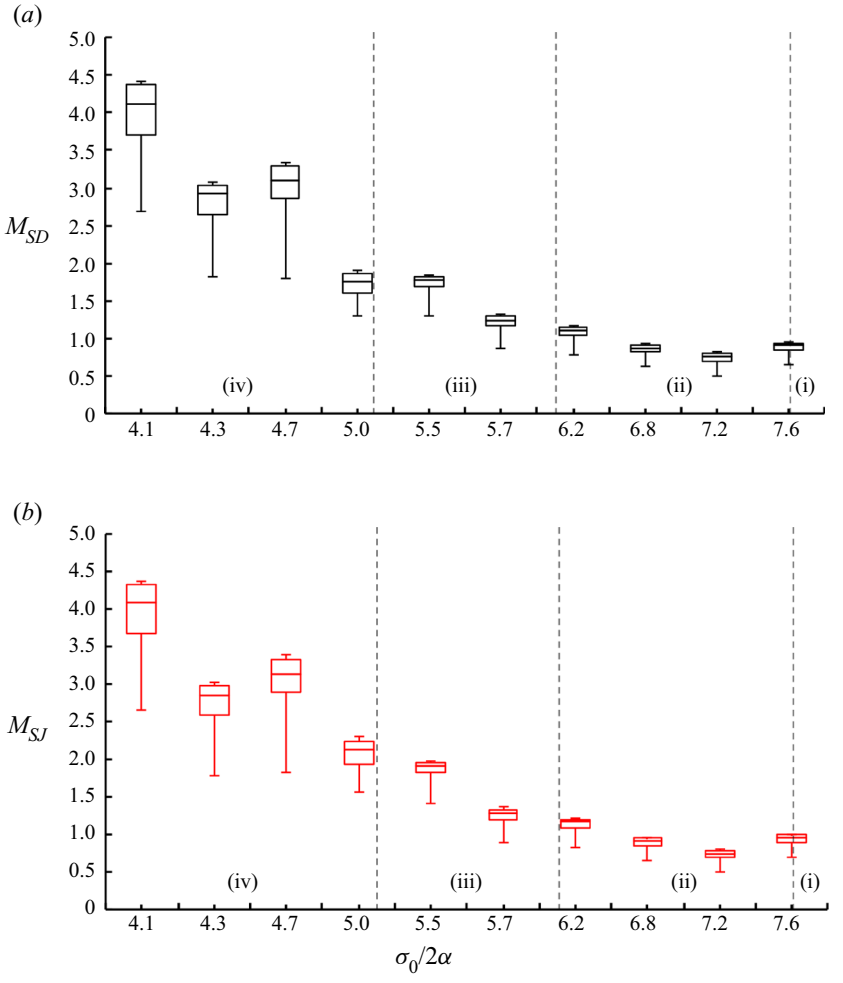

Figure 29. Box plot depicting variation of the peak value of M_S that occurs over multiple shedding cycles with decreasing $\sigma_0/2\alpha$. The boxes represent the median, the 75th and 25th percentiles, and the whiskers represent the maximum and minimum values. The data from the direct measurement of the shock speed and from those inferred from the jump conditions are both shown, where (*a*) M_{SD} were determined from the directly measured shock speed, and (*b*) M_{SJ} were computed using the jump condition, (8.1).

here M_S allows us to compare the shock propagation speed with our estimate of the mixture sound speed at the time of shock formation and propagation. Figure 29 presents M_S varying with $\sigma_0/2\alpha$ as a box plot. The shock speed u_S can be determined directly from the $s-t$ diagrams and from one-dimensional jump relations based on pressure measurements from $\mathrm{d}p_1$. The data from the direct measurement of the shock speed and from those inferred from the jump conditions are both shown, where M_{SD} is determined from the directly measured shock speed and M_{SJ} were computed using the jump condition, (8.1). The onset of type (ii) cavities have $M_S < 1$, but as $\sigma_0/2\alpha$ is reduced, the Mach number increases, crossing the $M_S = 1$ boundary.

The onset of supersonic cavity conditions correlates with the increased probability of shock wave formation. Figure 30 shows a composite plot with the event probability of liquid re-entrant flow and bubbly shock waves along with the mean and standard deviation of M_0, M_{SD} and M_{SJ}. The trend in increasing probability of shock formation

https://doi.org/10.1017/jfm.2022.999 Published online by Cambridge University Press

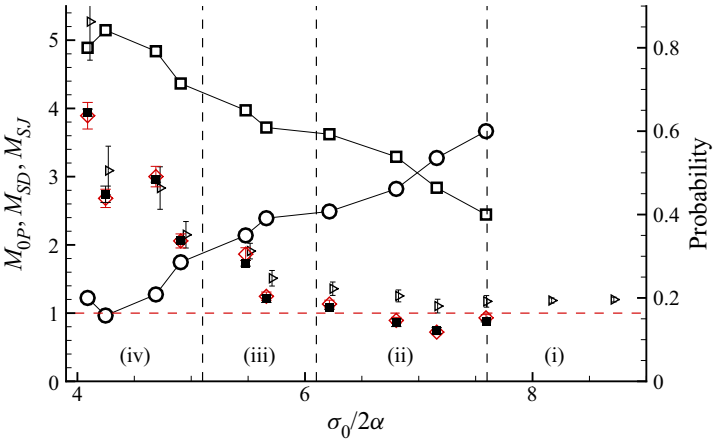

Figure 30. Variation of mean and standard deviation of M_{0P} (▷), M_{SD} (■), and M_{SJ} (red diamond) with $\sigma_0/2\alpha$. The event probability data $P(R)$ (◯) and $P(S)$ (□) are also shown. The horizontal dashed line demarcates where $M = 1$.

with increasing average Mach number is clearly observed. The Mach number defined with the local shock speed is lower than that defined with the inlet velocity, since the shock speed is often (but not always) lower than the free-stream speed. Here, M_S transitions from subsonic to supersonic near the value of $\sigma_0/2\alpha$ where there is equal probability of re-entrant flow or bubbly shock-induced shedding. The observation that the onset of shock formation corresponds to the transition from subsonic to supersonic conditions within the cavity is consistent with the observations of Bhatt *et al.* (2021).

10. Conclusions

We have examined the different partial cavity flow regimes on a two-dimensional NACA0015 hydrofoil using time-resolved X-ray densitometry and synchronized pressure measurements. We have shown that both re-entrant liquid jets and bubbly shock fronts can lead to cavity pinch-off and cloud formation. The classical understanding of the importance of re-entrant flows to cavity dynamics has been well documented by previous researchers, with the development of re-entrant flows resulting from the impingement of the liquid flow around the cavity on the solid flow boundary close to cavity closure. The existence and formation of such re-entrant flow are related to a number of factors, including the length and thickness of the cavity, the pressure gradients of the liquid flow in the closure region, and the degree of spanwise uniformity at the line of cavity closure. For nominally two-dimensional cavities, such re-entrant flow can lead to a near-wall liquid flow that is directed upstream toward the line of cavity detachment. And, when the flow impinges on the cavity interface, a cloud of vapour may be shed. Re-entrant flows can manifest over a wide range of cavitation numbers, and they can be present when the cavity is largely filled with vapour ($\beta \approx 1$) or when the pocket of separated flow contains a bubbly mixture.

The flow conditions that lead to the formation of a vaporous cavity can also produce a high void fraction bubbly mixture within the separated flow. If the void fraction of the mixture is very low ($\beta < 0.01$) or very high ($\beta \approx 1$), the sound speed of the mixture will likely be very large compared with the free-stream flow speed, making the cavity Mach number very low. Then, the effects of mixture compressibility can be neglected. However, if the void fraction of the bubbly cavity contents reaches values of the order of

https://doi.org/10.1017/jfm.2022.999 Published online by Cambridge University Press

$0.1 < \beta < 0.9$, the mixture sound speed falls to a value much lower than that of either the pure liquid or vapour. Bubbly shock fronts can then form within the cavity, and their upstream propagation can produce large-scale cavity pinch-off. The likelihood that either shedding mechanism will dominate is related to both the cavitation number and the Mach number within the cavity.

We have observed that the convection speed of the re-entrant flows and the propagation speed of the bubbly shock waves are often of the same order, reaching values close to that of the free-stream speed. This can make discerning the underlying mechanism of cavity shedding challenging when only using external visual imaging of the cavity. And, because re-entrant flow and shock convection speeds can be comparable, the shedding period that results from either mechanism may be similar. Yet, the mechanisms are distinct, and this is evidenced in multiple dominant frequencies and changes in the shedding rate that occurs with changes in flow conditions. These changes take place when the primary cloud formation mechanism transitions from re-entrant flow dominated to shock wave dominated shedding as the cavity flow changes from subsonic to supersonic.

Another distinction between re-entrant flow and bubbly shock-induced shedding is the influence of external pressure pulsations produced by shed vapour clouds on cavity dynamics. In the present study we see that the pressure pulse produced by the collapse of the shed cloud coincides with the initiation of the shock front at partial cavity closure when the cavity mixture Mach number is sufficiently large. The collapse of the shed cloud and its resulting pressure pulse thus become intimately linked to the cavity shedding cycle. Wu *et al.* (2019) and Barwey *et al.* (2020) on the other hand observed more complex interactions, when the collapsing cloud could interrupt the cavity growth before the cavity reached its maximum length. Observations in the present study indicate the presence of no multi-modality reported by Wu *et al.* (2019) and Barwey *et al.* (2020). Our test model was larger than Wu *et al.* (2019) and of similar scale to those of Kjeldsen *et al.* (2000), but both previous studies had different blockage and aspect ratios. Yet, there are remarkable differences in the cavity dynamics of the present study compared with these previous results. This may be due to the sensitivity of the flow to modest changes in the average static pressure in the liquid flow around the cavity. The pressure rise across the bubbly shock fronts was typically less than 10 kPa, or a modest multiple of the vapour pressure. The bubbly shock propagation process is sensitive to changes in the static pressure in the flow around the cavity that are of the order of the vapour pressure. Changes in blockage between two different but similar configurations can lead to slight increases or decreases in the static pressure near the cavity closure. Such modest variation in static pressure can then alter the cavity Mach number and shock propagation speed if the global pressure changes are at least of the order of the vapour pressure. Variations in static pressure distributions of this order were well within the range that we estimated as part of our blockage corrections for the cases studied here.

Supplementary movies. Supplementary movies are available at https://doi.org/10.1017/jfm.2022.999.

Funding. This work was supported by the Office of Naval Research under grant number N00014-18-1-2699, with Dr K.-H. Kim as Program Manager.

Declaration of interests. The authors report no conflict of interest.

Author ORCIDs.
Anubhav Bhatt https://orcid.org/0000-0002-6287-8156;
Harish Ganesh https://orcid.org/0000-0001-6230-6273.

https://doi.org/10.1017/jfm.2022.999 Published online by Cambridge University Press

References

ARNDT, R.E.A. 2012 Some remarks on hydrofoil cavitation. *J. Hydrodyn. Ser. B* **24** (3), 305–314.

ARNDT, R.E.A., SONG, C.S., KJELDSEN, M., HE, J. & KELLER, A. 2000 Instability of partial cavitation: a numerical/experimental approach. *Proceedings of the 23rd Symposium on Naval Hydrodynamics, Val de Reuil, France*, vol. 4. National Academies.

BARBACA, L., PEARCE, B.W., GANESH, H., CECCIO, S.L. & BRANDNER, P.A. 2019 On the unsteady behaviour of cavity flow over a two-dimensional wall-mounted fence. *J. Fluid Mech.* **874**, 483–525.

BARWEY, S., GANESH, H., HASSANALY, M., RAMAN, V. & CECCIO, S.L. 2020 Data-based analysis of multimodal partial cavity shedding dynamics. *Exp. Fluids* **61** (4), 1–21.

BHATT, A., GANESH, H. & CECCIO, S.L. 2021 Cavitating flow behind a backward facing step. *Intl J. Multiphase Flow* **139**, 103584.

BHATT, M. & MAHESH, K. 2020 Numerical investigation of partial cavitation regimes over a wedge using large eddy simulation. *Intl J. Multiphase Flow* **122**, 103155.

BRENNEN, C.E. 2005 *Fundamentals of Multiphase Flow*. Cambridge University Press.

BUDICH, B., SCHMIDT, S.J. & ADAMS, N.A. 2018 Numerical simulation and analysis of condensation shocks in cavitating flow. *J. Fluid Mech.* **838**, 759–813.

CALLENAERE, M., FRANC, J.-P., MICHEL, J.-M. & RIONDET, M. 2001 The cavitation instability induced by the development of a re-entrant jet. *J. Fluid Mech.* **444**, 223–256.

COUTIER-DELGOSHA, O., STUTZ, B., VABRE, A. & LEGOUPIL, S. 2007 Analysis of cavitating flow structure by experimental and numerical investigations. *J. Fluid Mech.* **578**, 171–222.

DE LANGE, D.F. & DE BRUIN, G.J. 1997 Sheet cavitation and cloud cavitation, re-entrant jet and three-dimensionality. *Appl. Sci. Res.* **58** (1), 91–114.

FRANC, J.P. 2001 Partial cavity instabilities and re-entrant jet. In *Proceeding of the 4th International Symposium on Cavitation*. HAL Open Science.

FURNESS, R.A. & HUTTON, S.P. 1975 Experimental and theoretical studies of two-dimensional fixed-type cavities. *J. Fluids Engng* **97** (4), 515–521.

GANESH, H., MAKIHARJU, S.A & CECCIO, S.L. 2016 Bubbly shock propagation as a mechanism for sheet-to-cloud transition of partial cavities. *J. Fluid Mech.* **802**, 37–78.

GOPALAN, S. & KATZ, J. 2000 Flow structure and modeling issues in the closure region of attached cavitation. *Phys. Fluids* **12** (4), 895–911.

JAHANGIR, S., HOGENDOORN, W. & POELMA, C. 2018 Dynamics of partial cavitation in an axisymmetric converging-diverging nozzle. *Intl J. Multiphase Flow* **106**, 34–45.

KAWANAMI, Y., KATO, H., YAMAGUCHI, H., TANIMURA, M. & TAGAYA, Y. 1997 Mechanism and control of cloud cavitation. *Trans. ASME J. Fluids Engng* **119** (4), 788–794.

KJELDSEN, M., ARNDT, R.E.A. & EFFERTZ, M. 2000 Spectral characteristics of sheet/cloud cavitation. *Trans. ASME J. Fluids Engng* **122** (3), 481–487.

KNAPP, R.T. 1955 Recent investigations of the mechanics of cavitation and cavitation damage. *Trans. ASME* **77**, 1045–1054.

LABERTEAUX, K.R. & CECCIO, S.L. 2001*a* Partial cavity flows. Part 1. Cavities forming on models without spanwise variation. *J. Fluid Mech.* **431**, 1–41.

LABERTEAUX, K.R. & CECCIO, S.L. 2001*b* Partial cavity flows. Part 2. Cavities forming on test objects with spanwise variation. *J. Fluid Mech.* **431**, 43–63.

LE, Q., FRANC, J.-P. & MICHEL, J.-M. 1993 Partial cavities: global behavior and mean pressure distribution. *Trans. ASME J. Fluids Engng* **115** (2), 243–248.

LEROUX, J.-B., ASTOLFI, J.A. & BILLARD, J.Y. 2004 An experimental study of unsteady partial cavitation. *Trans. ASME J. Fluids Engng* **126** (1), 94–101.

LEROUX, J.-B., COUTIER-DELGOSHA, O. & ASTOLFI, J.A. 2005 A joint experimental and numerical study of mechanisms associated to instability of partial cavitation on two-dimensional hydrofoil. *Phys. Fluids* **17** (5), 052101.

MÄKIHARJU, S.A., GABILLET, C., PAIK, B.-G., CHANG, N.A., PERLIN, M. & CECCIO, S.L. 2013*a* Time-resolved two-dimensional X-ray densitometry of a two-phase flow downstream of a ventilated cavity. *Exp. Fluids* **54** (7), 1–21.

MÄKIHARJU, S.A., PERLIN, M. & CECCIO, S.L. 2013*b* Time resolved X-ray densitometry for cavitating and ventilated partial cavities. *Intl Shipbuilding Prog.* **60** (1–4), 471–494.

PETKOVŠEK, M., HOČEVAR, M. & DULAR, M. 2020 Visualization and measurements of shock waves in cavitating flow. *Exp. Therm. Fluid Sci.* **119**, 110215.

PHAM, T.M., LARRARTE, F. & FRUMAN, D.H. 1999 Investigation of unsteady sheet cavitation and cloud cavitation mechanisms. *Trans. ASME J. Fluids Engng* **121** (2), 289–296.

https://doi.org/10.1017/jfm.2022.999 Published online by Cambridge University Press

SMITH, S.M., VENNING, J.A., PEARCE, B.W., YOUNG, Y.L. & BRANDNER, P.A. 2020 The influence of fluid–structure interaction on cloud cavitation about a stiff hydrofoil. Part 1. *J. Fluid Mech.* **896**, A1.

TRUMMLER, T., SCHMIDT, S.J. & ADAMS, N.A. 2020 Investigation of condensation shocks and re-entrant jet dynamics in a cavitating nozzle flow by large-eddy simulation. *Intl J. Multiphase Flow* **125**, 103215.

WADE, R.B. & ACOSTA, A.J. 1966 Experimental observations on the flow past a plano-convex hydrofoil. *J. Basic Engng* **88** (1), 273–282.

WU, J., DEIJLEN, L., BHATT, A., GANESH, H. & CECCIO, S.L. 2021 Cavitation dynamics and vortex shedding in the wake of a bluff body. *J. Fluid Mech.* **917**, A26.

WU, J., GANESH, H. & CECCIO, S.L. 2019 Multimodal partial cavity shedding on a two-dimensional hydrofoil and its relation to the presence of bubbly shocks. *Exp. Fluids* **60** (4), 1–17.

https://doi.org/10.1017/jfm.2022.999 Published online by Cambridge University Press